RECLAMATION

Managing Water in the West

Desalination and Water Purification Research
and Development Program Report No. 214

An Integrated Photoelectrochemical Zero Liquid Discharge System for Inland Brackish Water Desalination

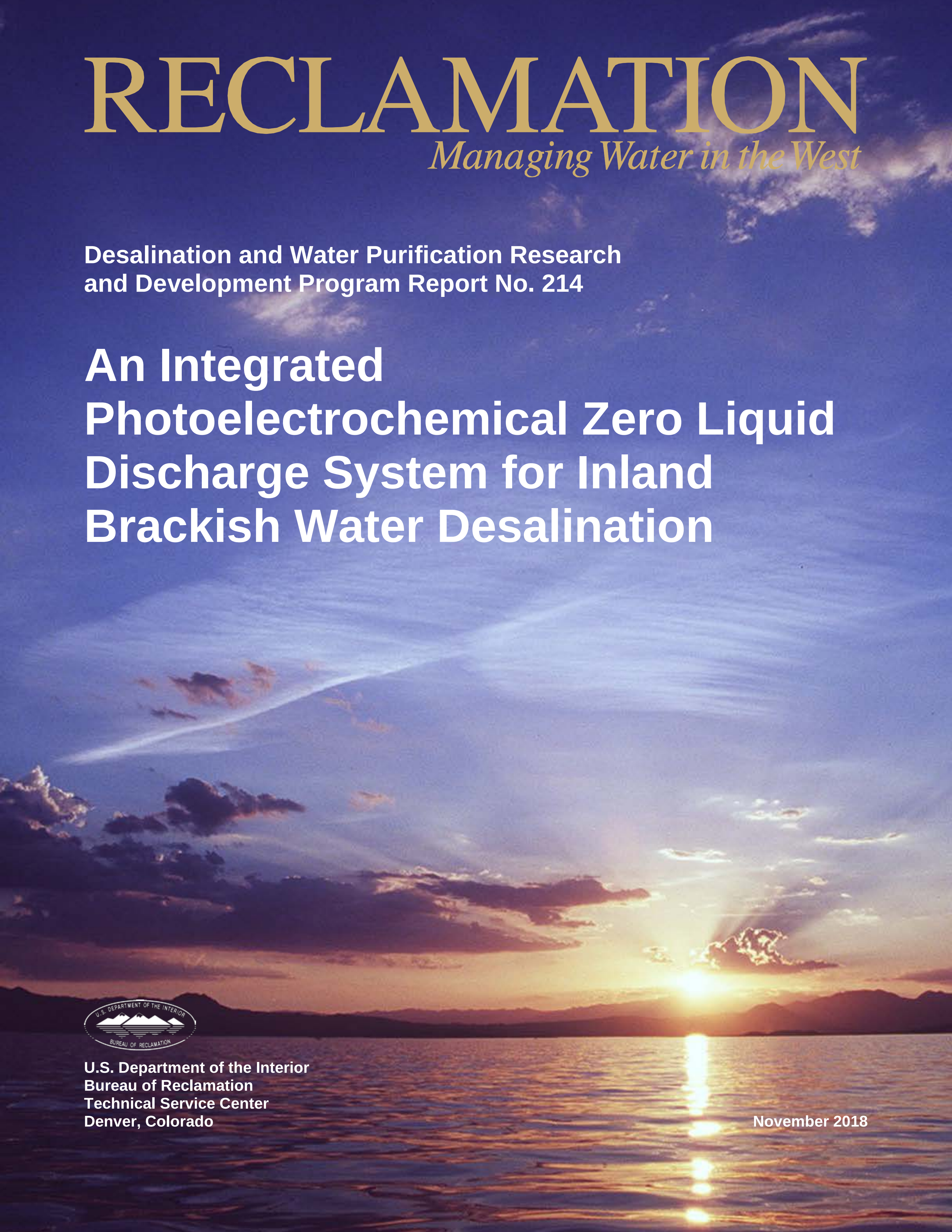

U.S. Department of the Interior
Bureau of Reclamation
Technical Service Center
Denver, Colorado

November 2018

REPORT DOCUMENTATION PAGE	*Form Approved* *OMB No. 0704-0188*

1. REPORT DATE *(DD-MM-YYYY)* 09/17/2018	2. REPORT TYPE Final	3. DATES COVERED *(From - To)* 09/01/2016 – 09/01/2018

4. TITLE AND SUBTITLE An Integrated Photoelectrochemical Zero Liquid Discharge System for Inland Brackish Water Desalination	5a. CONTRACT NUMBER Agreement No. R16AC00126
	5b. GRANT NUMBER
	5c. PROGRAM ELEMENT NUMBER
6. AUTHOR(S) Dr. Syed Mubeen Assistant Professor, Chemical and Biochemical Engineering University of Iowa 319-335-5813, syed-mubeen@uiowa.edu	5d. PROJECT NUMBER
	5e. TASK NUMBER
	5f. WORK UNIT NUMBER
7. PERFORMING ORGANIZATION NAME(S) AND ADDRESS(ES) University of Iowa Department of Chemical and Biochemical Engineering 4133 Seamans Center Iowa City, Iowa 52242	8. PERFORMING ORGANIZATION REPORT NUMBER
9. SPONSORING/MONITORING AGENCY NAME(S) AND ADDRESS(ES) Bureau of Reclamation U.S. Department of the Interior Denver Federal Center PO Box 25007, Denver, CO 80225-0007	10. SPONSOR/MONITOR'S ACRONYM(S) Reclamation
	11. SPONSOR/MONITOR'S REPORT NUMBER(S) DWPR Report No. 214

12. DISTRIBUTION/AVAILABILITY STATEMENT
Online at https://www.usbr.gov/research/dwpr/DWPR_Reports.html

13. SUPPLEMENTARY NOTES

14. ABSTRACT

This project evaluated the feasibility of an integrated sunlight-driven zero liquid discharge (ZLD) system for inland brackish desalination, with the simultaneous production of fuels and chemicals. The process uses NaCl rich concentrate (concentrations similar to brine produced from an reverse osmosis (RO) desalination unit) in a photoelectrochemical (PEC) reactor equipped with photoelectrodes and electroactive membranes to generate marketable chemicals such as hydrogen (H_2), chlorine (Cl_2) and sodium hydroxide (NaOH) using sunlight as the energy input

The results demonstrate that photocathodes and photoanodes made of earth-abundant elements – i.e., elements found abundant in earth's crust (e.g., tin sulfide and bismuth vanadate) - can be engineered to produce H_2 and Cl_2 sustainably using sunlight as the energy input. The report also outlines the development of novel electroactive membranes to address membrane scaling and fouling issues. A technoeconomic analysis of the entire PEC system to identify key performance targets for cost-effective operation is also presented. The sensitivity analysis indicated that the efficiency of the photoelectrodes plays a crucial role in affecting the overall cost reduction for the proposed integrated ZLD system.

15. SUBJECT TERMS
Zero Liquid Discharge, Photoelectrochemical Reactor, Solar H_2 production, Chloralkali Process, Electroactive Membranes

16. SECURITY CLASSIFICATION OF:			17. LIMITATION OF ABSTRACT	18. NUMBER OF PAGES	19a. NAME OF RESPONSIBLE PERSON Scott Irvine
a. REPORT U	b. ABSTRACT U	THIS PAGE U			19b. TELEPHONE NUMBER *(Include area code)* 303-445-2253

Desalination and Water Purification Research and Development Program Report No. 214

An Integrated Photoelectrochemical Zero Liquid Discharge System for Inland Brackish Water Desalination

Prepared for the Bureau of Reclamation Under Agreement No. R16AC00126

By

Dr. Syed Mubeen
Assistant Professor
Chemical and Biochemical Engineering
University of Iowa

U.S. Department of the Interior
Bureau of Reclamation
Technical Service Center
Denver, Colorado

November 2018

Mission Statements

The Department of the Interior conserves and manages the Nation’s natural resources and cultural heritage for the benefit and enjoyment of the American people, provides scientific and other information about natural resources and natural hazards to address societal challenges and create opportunities for the American people, and honors the Nation’s trust responsibilities or special commitments to American Indians, Alaska Natives, and affiliated island communities to help them prosper.

The mission of the Bureau of Reclamation is to manage, develop, and protect water and related resources in an environmentally and economically sound manner in the interest of the American public.

Disclaimer

The views, analysis, recommendations, and conclusions in this report are those of the authors and do not represent official or unofficial policies or opinions of the United States Government, and the United States takes no position with regard to any findings, conclusions, or recommendations made. As such, mention of trade names or commercial products does not constitute their endorsement by the United States Government.

Acknowledgments

The Desalination and Water Purification Research and Development Program, Bureau of Reclamation sponsored this research.

Acronyms and Abbreviations

3-D	three-dimensional
AC	alternating current
AAO	anodic aluminum oxide
ALD	atomic layer deposition
AM	atmospheric mass
BGNDRF	Brackish Groundwater National Desalination Research Facility
CB	conduction band
CBD	chemical bath deposition
CdS	cadmium sulfide
DI	deionized
DLD	delay-line detector
DSIMS	dynamic secondary ion mass spectroscopy
E_{CB}	conduction band edge energy
ED	electrical dialysis
EDS	energy-dispersive x-ray spectroscopy
E_{VB}	valence band energy
FEI	field electron and ion company
FFT	fast Fourier transform
FTO	fluorine-doped tin oxide
GC	gas chromatography
H2A	hydrogen production analysis
HRTEM	high resolution transmission electron microscopy
IPA	isopropyl alcohol
IPCE	incident photon-to-electron conversion efficiency
IQE	internal quantum efficiency
IR	infrared
LSV	linear sweep voltammetry
MACRS	Modified Accelerated Cost Recovery System
MCD	multi-channel detector
MSF	multi-stage flash
MPD	multipurpose diffractometer
NF	nanofiltration
PAN	polyacrylonitrile
PEC	photoelectrochemical
P_{in}	incident power
Pt	platinum
PV	photovoltaic
RO	reverse osmosis
Reclamation	Bureau of Reclamation
RFS	relative sensitivity factor
RHE	reversible hydrogen electrode
SCE	saturated calomel electrode
SEM	scanning electron microscopy
SIMS	secondary ion mass spectrometry

TDMAT	tetrakis(dimethylamino)titanium
TDS	total dissolved solids
TEA	triethanolamine
TEM	transmission electron microscopy
UV-Vis	ultraviolet–visible spectrophotometry
XPS	x-ray photoelectron spectroscopy
XRD	x-ray diffraction
ZLD	zero liquid discharge

Measurements

°C	degree Celsius
Å	angstrom
cm	centimeter
cm^2	square centimeter
eV	electron volt
g	gram
kg	kilogram
kHz	kilohertz
kWh	kilowatt hour
kWh/m^3	kilowatt hours per cubic meter
kWh/ton	kilowatt hours per ton
kV	kilovolt
M	molar
m^3	cubic meter
mbar	millibar
mA	milliamp
mA/cm^2	milliamps per square centimeter
mC/cm^2	millicoulombs per square centimeter
ml	millliter
mm	millimeter
mM	milliMolar
ms	millisecond
mW/cm^{-2}	milliwatts per square centimeter
mV	millivolt
mV/s	millivolts per second
nm	nanometer
ppm	parts per million
P_{in}	incident light power density
V	volt
W	watt
wt%	percent by weight
$\mu A/cm^2$	microamps per square centimeter
µg/L	micrograms per liter
µL	microliter
µm	micron

Contents

Figures

Tables

Executive Summary

Surging population, energy demands, and climate change will push us, ever more urgently, to find new approaches to meet growing water demands. Most often, this will involve harvesting lower quality or impaired water supplies (e.g., seawater or brackish groundwater) as a source for drinking water. Recently desalination using membrane-based processes (e.g., reverse osmosis [RO], electrodialysis [ED], and nanofiltration [NF]) has shown promise for providing additional sources of fresh water across the United States. However, the current membrane separation processes are commonly energy intensive and produce large volumes of concentrated brine which poses unique challenges. Particularly in land-locked urban center brine disposal often relyes on surface water discharge or deep-well injection which pose economic and practical difficulties for wide-spread adoption of such technologies. Thus, there is an urgent need for energy-efficient desalination technologies that reduce the amount of concentrate produced, or identify cost-effective solutions for concentrate management.

The overall goal of this study is to demonstrate and evaluate the feasibility of an integrated sunlight-driven zero liquid discharge (ZLD) system for inland brackish desalination, with simultaneous production of fuels and chemicals (Figure ES-1).

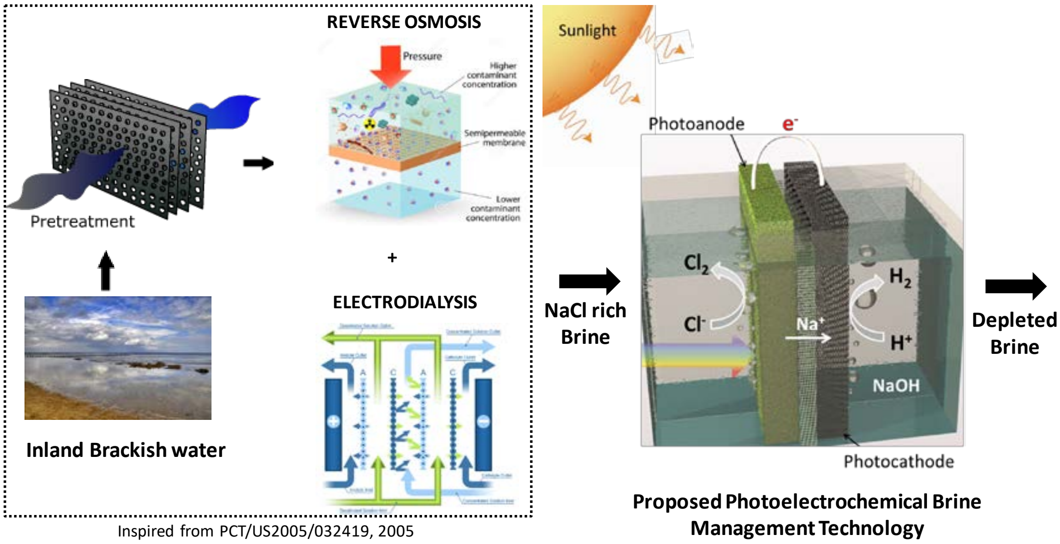

Figure ES-1. Summary of the proposed integrated sunlight-driven ZLD desalination system.

This approach uses NaCl rich concentrate produced from an integrated RO/ED unit (inspired by Davis 2005) to generate marketable H_2, Cl_2, and NaOH, using a photoelectrochemical (PEC) reactor with sunlight as the only energy input.

Specifically, the study addresses two key innovations:

1. **Replacing evaporation ponds with earth abundant, high-efficient, nanostructured photo-active solids** (e.g., tin sulfide [SnS] and bismuth vanadate [$BiVO_4$]) that use photon energy in sunlight for electrolyzing NaCl rich concentrates ($NaCl + H_2O \rightarrow H_2 + Cl_2 + NaOH$). The H_2 produced could be used for *in-situ* electricity generation (using fuel cells) for the plant or sold as a commodity chemical, the Cl_2 could be used for processing feed water or could be sold as a disinfectant, and the NaOH could be used for salt recovery.

2. **Developing low cost, electrically conductive, ion-exchange membranes** with tunable porosity, wettability, and ion-selectivity that can induce periodic electrostatic repulsive forces to prevent precipitation of divalent ions (Ca^{2+}/SO_4^{2-}) at the membrane surface.

This study is based on the premise that:

- Using solar energy to generate valuable products from membrane concentrate will minimize the concentrate volume and lower the overall cost and carbon footprint of desalination technologies.

- Using electrically conductive inorganic membranes to prevent membrane scaling issues will minimize the number of pretreatment steps needed, subsequently reducing the primary energy use and the amount of concentrate brines produced.

The report contains results on the above innovations and is categorized under four primary tasks:

1. **Develop and stably operate novel photoelectrodes for Cl_2 and H_2 evolution.** We synthesized semiconductor electrodes made of earth-abundant non-toxic materials on transparent conducting substrates and characterized these for solar driven H_2 and Cl_2 production. For solar H_2 production, highly photoactive tin sulfide (SnS) nanoplatelets were fabricated by low-cost chemical bath deposition (CBD). Protected by an atomic-layer-deposited titanium oxide layer, the best performing tin sulfide photocathodes produced H_2 with photocurrent densities reaching 2.5 milliamps per square centimeter (mA/cm^2) at the reversible hydrogen evolution potential under simulated visible light illumination (wavelengths (λ) > 500 nanometers [nm], incident light power density (P_{in}) = 80 milliwatts per square centimeter [$mW\ cm^{-2}$]). Note: A xenon lamp source with appropriate filters was used to simulate sunlight, and a thermopile detector was used to measure light power density. The internal quantum efficiency averaged over the entire solar spectrum at 0 volts (V) vs. reversible hydrogen electrode (RHE) was ~13%.

We also demonstrated using bismuth vanadate for photoelectrochemical production of chlorine gas from acidified sodium chloride solution. An amorphous tungsten oxide protective layer was electrochemically deposited on the nanoporous bismuth vanadate to prevent photo-corrosion of bismuth vanadate during electrochemical operation. The best performing material showed stable operation for chlorine production at 2 mA/cm^2.

2. **Develop and evaluate the performance of novel inorganic, electrically conducting, fouling-resistant membranes.** Two types of inorganic membranes were synthesized and characterized:

    a. Hollow inorganic membrane architecture, consisting of vertical arrays of carbon nanotubes inside porous anodic aluminum oxide (AAO) membranes.

    b. Porous inorganic membrane architectures consisting of vertical arrays of nanoporous metal nanowires inside anodic aluminum oxide (AAO) membranes. The nanoporous metal membranes demonstrated superior performance for selective passage of cations or anions by controlling the membrane surface charge density as a function of the applied bias. The non-optimized membranes showed cation selectivity (K^+/Cl^-) of about 6 and anion selectivity (Cl^-/K^+) of about 3, depending on the magnitude of the applied bias. The membranes also showed improved fouling resistance in highly concentrated brines after 100 hours of operation.

3. **Demonstrate the proposed process for lab-scale treatment of concentrated brines.** The electrodes were tested in a lab-scale brine management unit, and feasibility of its autonomous operation using sunlight as the sole energy input was demonstrated.

4. **Conduct a technical and economic assessment of the overall process**. A technoeconomic analysis was developed for the tested PEC ZLD discharge system. The preliminary calculations indicated that the efficiency of the photoelectrodes is the significant cost reduction factor for the overall operation and that sales of the H_2, Cl_2, and NaOH could not only offset the added cost of the ZLD process but could favorably reduce the total freshwater production cost.

1. Introduction

1.1. Project Background

1.1.1. Problem

As the population grows and climate changes, the science and engineering community will need to develop cost-effective, energy-efficient ways of treating impaired water with minimum environmental impact. Fueled to a great extent by Federal investments and advancements in material science and engineering, the concept of desalination—producing fresh water from sea water or brackish inland water—has become a realistic option for clean water production. However, the largest market and most significant societal benefit can only be addressed when the energy consumption cost and concentrate management cost for producing fresh water is less than the levelized cost of electricity generation, or approximately \$0.05-\$0.2/ per kilowatt hour (kWh) (Logan et al. 2017).

However, current inland desalination technologies are hindered by concerns over their long-term cost, energy, and environmental sustainability. State-of-the-art medium-to-large scale desalination technologies are listed in Table 1**.** These are mainly based on membrane separation and thermal distillation, of which RO accounts for >50% (Khawaji et al. 2008 and Peñate and García-Rodríguez 2012). Particularly in the arid Southwest, there is growing reliance on wastewater recycling where high-pressure membrane processes are used to restore municipal and industrial wastewater to a quality suitable for beneficial reuse (including drinking). Brackish or contaminated groundwater aquifers are increasingly used to bridge the ever-widening gap between supply and demand. Although the amount of power to run current RO desalination plants has significantly decreased in the past few decades, the concentrated brine produced as a result of inland brackish desalination could create a significant economic and environmental problem if it is not adequately managed (Elimelech and Phillip 2011).

Table 1. Performance Metrics for Leading Desalination Technologies (Kim et al. 2010, Shrestha et al. 2011, Karagiannis and Soldatos 2008, and Kesieme et al. 2013)

Systems	Total Energy Consumption (kWh/m^3)	Freshwater cost (\$/m^3)	Lifecycle cost (Energy cost /membrane lifetime)	$kgCO_2$ emissions per m^3 of desalted water
RO	2.5-4.0	0.5-3.0	Very High	1.78
ED	0.3-2.8	1.0-3.5	High	~1-2
Thermal distillation	6-15.0	0.7-4.00	NA	23.41

kWh/m^3 = kilowatt-hours per cubic meter
m^3 = cubic meter
$kgCO_2$ = kilograms of carbon dioxide

Cost-effective, environmentally sustainable, concentrate management options will dictate inland brackish water desalination. Concentrate management for desalination residuals mainly involves brine disposal, of which surface waters and sewers discharge accounts for more than 70 percent. Although surface water discharge costs less and is less energy intensive, its potential environmental impacts on aquatic life and downstream water sources make large volume disposal unsuitable. Currently, only thermal evaporation systems provide environmentally sustainable zero-liquid discharge (ZLD) concentrate management options by maximizing water usage and minimizing waste disposal (Table 2). However, their deployment for municipal applications is currently limited due to their prohibitive capital and operation cost.

To lower the overall process cost for ZLD, recent efforts have focused on producing positive value-added products by integrating ED and evaporation/crystallization system to RO (Davies 2005) or multi-stage flash (MSF) distillation units (Turek 2003). Electrodialysis was used to improve NaCl recovery from RO concentrate, while evaporation/crystallization stage concentrated more than 75% of NaCl in ED brine as marketable NaCl crystals (Davies 2005). While the thermal energy needed for evaporation is reduced, such an approach will still require high evaporation rates to offset the cost associated with liners (to prevent seeping) for large surface area ponds.

Table 2. Current Concentrate Management Options for Inland Desalination in Comparison to the Proposed Technology (Karagiannis et al. 2008, Shrestha et al. 2011, and Kesieme et al. 2013)

Systems	Capital + Operation & Maintenance cost	Environmental Impact	Energy use
Surface water/Sewer discharge	Low	Medium/High	Low
Deep-well Injection	Medium/High	Low/Medium	High
Thermal Evaporation	High	Low	High
(Proposed Technology)	**Low (*Cost offset due to valuable product generation)**	**Low**	**Very low**

1.1.2. Needs

ZLD desalination system sustainability can be improved by integrating sunlight-driven electrochemical technologies. Using the electrochemical process for concentrate management offers several advantages:

1. The electrochemical process allows the generation of higher value chemicals and products from membrane concentrate than from thermal evaporation. For example, one could electrolyze NaCl rich concentrate to selectively produce Cl_2, H_2, and NaOH (chloralkali process). Chlorine, H_2, and NaOH, each sells for nearly $500/ton compared to $40 to 100/ton for NaCl crystals.

2. Electrochemical process can be performed at ambient temperature and pressure.

3. Ease of integration to renewable energy offers treatment possibilities at off-grid locations.

4. Modular nature of the process offers ease of scalability.

Despite the useful and essential features of electrochemical-based processes, current methodologies have some shortcomings for brine treatment. For example, the amount of energy invested in creating a product (measured in kilowatt-hours per ton [kWh/ton]) is very high for electrochemical processes. To produce one ton of Cl_2 from 36 percent by weight (wt%) NaCl, the amount of energy required for a membrane is driven electrolysis process is approximately 2,500-kilowatt hours (kWh) (Note: 1 ton of Cl_2 produces 1.1 tons of NaOH and 28 kg of H_2). These energy requirements are likely to increase as NaCl concentrations decrease in the residual brine, making these electrolyzers too expensive for practical implementation. Further, it has been shown that presence of divalent ions (Ca^{2+}, Mg^{2+}, SO_4^{2-}) even in minute quantities (<10 parts per million [ppm]) increases the electrical resistance of both RO and ion-exchange membranes, causes membrane fouling, and decreases the overall electrochemical-to-product conversion efficiency.

1.1.3. Objectives

To address the above challenges, this study addressed two research and development objectives:

1. Integrating solar-powered electrochemical reactors to provide all or part of the energy required for product formation. The proposed process will convert photon energy in sunlight to chemical potential energy by driving electrochemical reactions, which will generate fuels and chemicals from concentrate. Specifically, the proposed approach integrates sunlight powered electrode assemblies directly into a concentrate treatment unit to produce hydrogen, chlorine, and sodium hydroxide (Figure 1).

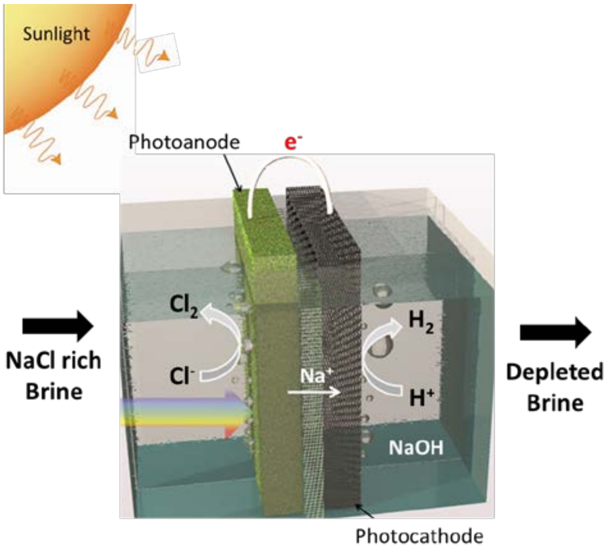

Figure 1.—Proposed solar energy powered photoelectrochemical concentrate management technology.

2. Developing inorganic, electrically conducting membranes to overcome membrane fouling issues and concentration polarization losses. Current membranes used for electrolysis such as chloralkali process requires stringent electrolyte requirements. The presence of divalent ions—even in quantities less than 100 ppm—significantly affects the overall performance of the electrochemical reactor. To address this challenge, we developed a novel electrically conducting inorganic membrane with tunable properties that can be integrated into standard perfluorinated chloralkali membrane unit (Figure 2). The synthesized membranes can be periodically triggered with direct current (DC) voltage to impart ion-selectivity and can also cause electrostatic repulsion of divalent ions away from the membrane surface to overcome concentration polarization losses and membrane fouling issues (Bowen et al. 1989 and Jagannadh and Muralidhara 1996). Although not investigated in this study, electrical triggering can also be used to enhance ion flux across the membranes.

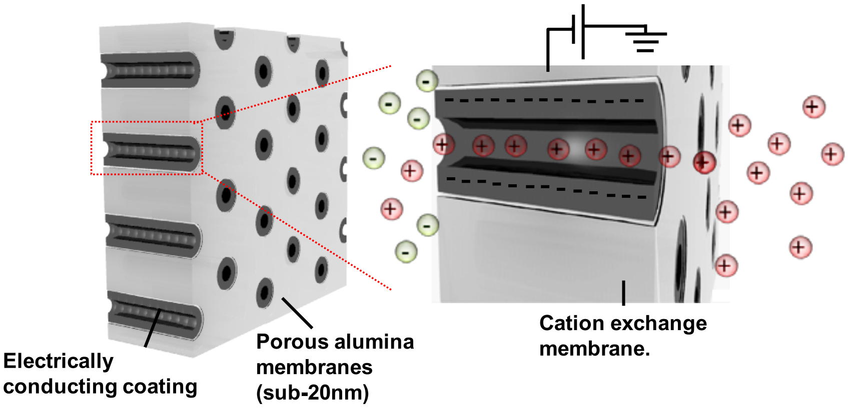

Figure 2.—Schematic of inorganic electrically conducting membranes containing hollow electrically conductive coatings inside a porous alumina membrane.

1.2. Project Overview

1.2.1. Overall Approach

To confront the challenges of desalination at the energy-water-environment nexus, we tested an innovative, integrated photoelectrochemical zero-liquid discharge desalination system. Effectively, the proposed process would take a negative value feedstock (concentrate from desalination plants) and convert it to high-value commodity chemicals (hydrogen, chlorine and sodium hydroxide) using an environmentally and economically sustainable platform. A block flow diagram of the proposed integrated PEC/ZLD system is shown in Figure 3.

The pretreated brackish water is first reacted with sodium carbonate and barium chloride to precipitate calcium and sulfates (Note: inland brackish water sources have higher calcium to sodium and sulfate to chloride ratios than sea water and thus calcium and sulfates should be removed before photoelectrochemical reaction). The magnesium ions could be precipitated using sodium hydroxide produced from the photo-electrochemical process. The salt recovery steps might also precipitate different metal ions such as iron, nickel, etc. After the salt recovery stage, the pretreated water (now predominant with sodium chloride) is passed through a combined RO/ED unit as proposed by Davies (2005). Because of the strong rejection nature of divalent ions from the ED unit, the concentrate after pretreatment/RO/ED stages will have high sodium chloride concentration. The sodium chloride rich concentrate is then acidified and fed to the PEC reactor integrated with electrically conducting membranes to produce hydrogen, chlorine, and sodium hydroxide. Chlorine could be used to treat ED membranes or sold as a disinfectant, hydrogen can be used to supply electricity to the desalination plant by running through a fuel cell stack, and sodium hydroxide can be sold or used for salt recovery. Depleted brine can be concentrated and fed back to the PEC reactor.

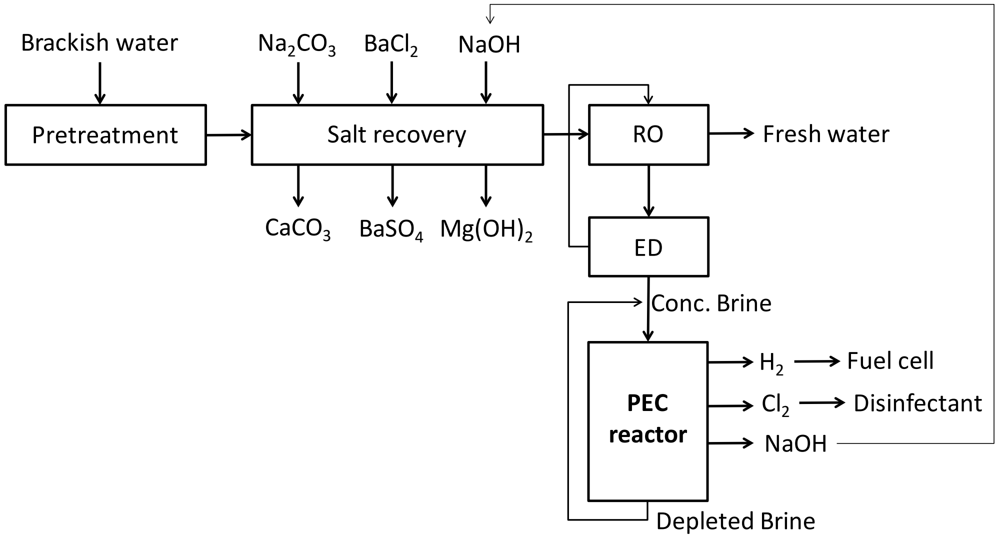

Figure 3.—Proposed block flow diagram for sunlight driven zero liquid discharge desalination system.

For this project, we focused on developing and evaluating the feasibility of a photoelectrochemical reactor to treat membrane concentrate from the inland brackish desalination plant. Our ultimate goal was to improve the cost and energy efficiency of brine management by integrating highly efficient fuel-producing photoactive solids and electrically conducting, nanostructured inorganic membranes.

1.2.2. Working Concept

An exploded view of our basic unit is shown in Figure 4(a). The unit consists of two electrodes: a p-type semiconductor photocathode (negative electrode) to drive the reduction reaction ($H^+ + e^- \rightarrow \frac{1}{2}H_2$) and an n-type semiconductor photoanode (positive electrode) to drive the oxidation reaction ($Cl^- \rightarrow \frac{1}{2}Cl_2 + e^-$).

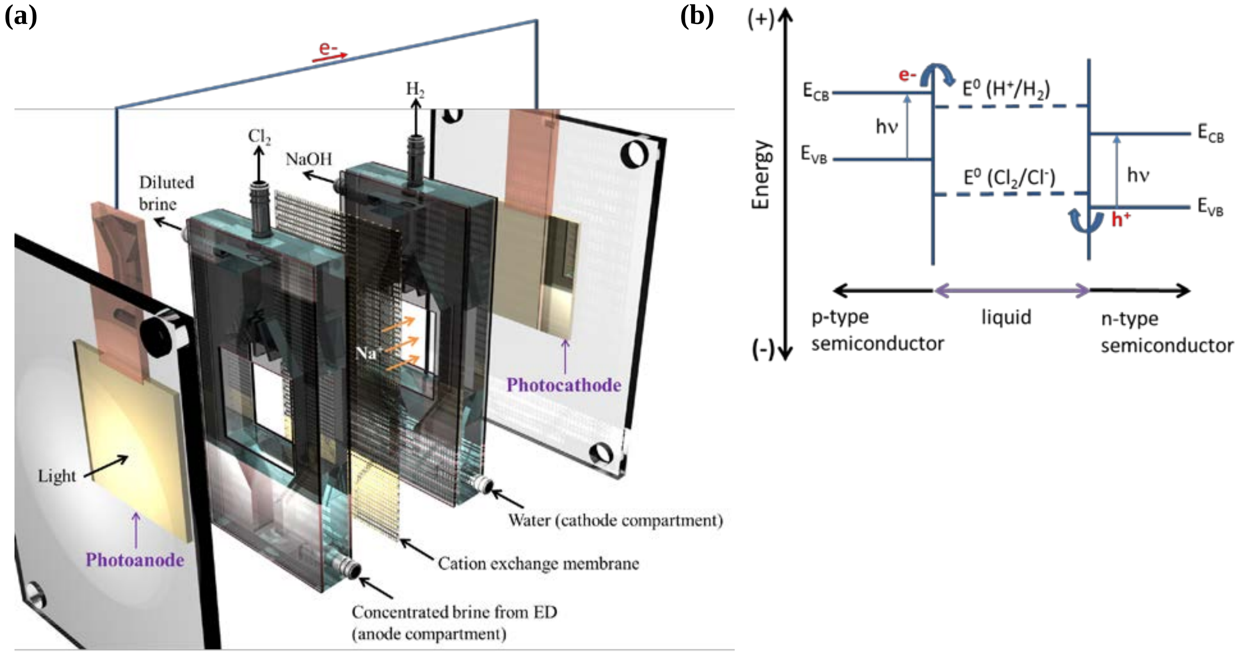

Figure 4.—(a) Expanded view of the photoelectrochemical cell. (b) Energy diagram for a p-type and n-type photoelectrode in contact with electrolyte under illumination. E^0 is the electrochemical potential and e- and h+ are electrons and holes (positive charges) taking part in the reaction.

The two photoelectrodes are placed in different compartments separated from each other by a water impermeable ion-exchange membrane. The concentrated brine from the ED units is introduced into the anode compartment where chloride ions are oxidized by the photoanode to chlorine gas. The electrons generated as a result of this reaction will transfer through the external circuit to the negative electrode compartment where water is electrolyzed to hydrogen gas and hydroxyl ions by the photocathode. The sodium ions migrate from the anode compartment to the cathode compartment through the ion exchange membranes to maintain charge balance. The ion-exchange membrane prevents mixing of solutions across each compartment while allowing the selective transfer of ions to maintain electroneutrality. Depleted brine is discharged from the anode compartment, hydrogen and chlorine gas is collected from their respective compartments, and the sodium hydroxide in solution could be crystallized or can be used in the desalination plant for precipitating magnesium salts.

It should be noted that for hydrogen production, the p-type semiconductor's conduction band edge energy (E_{CB}) should be more positive than the electrochemical potential for hydrogen production (E^0 (H^+/H_2); Figure 4(b) for efficient charge transport. Similarly, for chlorine production, the n-type semiconductor's valence band energy (E_{VB}) should be more negative than the electrochemical potential for chlorine production (E^0 (Cl_2/ Cl^-)). The proposed photoelectrodes (tin sulfides for hydrogen production and bismuth vanadate for chlorine production) satisfy these interfacial energetics criteria.

2. Technical Approach and Methods

2.1. Approach for Photoelectrodes

The specific objective is to demonstrate the capability to synthesize high-efficient photoelectrodes (both p-type and n-type) using earth abundant materials with the appropriate structure-property relationship for efficient and stable sunlight-driven electrolysis of concentrated brines. The focus was on nanostructured materials to enhance light absorption, carrier transport, and reaction rates. We accomplished this by depositing semiconductor absorbers on transparent conducting oxide substrates. We employed a variety of growth methods to synthesize these photoelectrodes, including chemical bath deposition, physical vapor deposition, and electrodeposition to create complex absorbing materials with complex geometries on top of the conducting substrates.

Different band gap p-type and n-type photoelectrodes were synthesized and characterized for concentrate treatment. We developed and characterized tin sulfide (E_g = 1.1 eV) as a p-type photocathode and bismuth vanadate (E_g = 2.00 eV) as an n-type photoanode. Tin sulfide was coated with nanometer-thick platinum (Pt) layers which served as the electrocatalyst for hydrogen production, and bismuth vanadate was coated with a tungsten oxide electrocatalyst for chlorine evolution. The bandgap of the two photoelectrodes allows one to connect these electrodes optically in series so that:

Step 1. The light first hits the semiconductor with a higher band gap; in this case, bismuth vanadate (Figure 5).

Step 2. The harvested light by bismuth vanadate (<600 nm) is then spatially separated as electron/hole pairs through an inherent built-in potential formed between the semiconductor electrolyte interface. Note: electrons are negatively charged, and holes are positively charged.

Step 3. The spatially separated charges are then transferred to electrocatalytic elements of the structure.

Step 4. The holes oxidize chloride ions to produce chlorine in the anode chamber which is then removed from the photoreactor.

Step 5. The lower bandgap semiconductor then absorbs the light not absorbed by the higher bandgap semiconductor (600 - 1,130 nm) to perform complementary hydrogen production reaction.

2.2. Approach for Ion-exchange Membranes

Typically, the membranes used for chloralkali production are perfluorinated cation-exchange polymeric membranes, through which only monovalent Na^+ ions can pass through. The anode side of the membrane has sulfonic groups while the cathodic side has carboxylic groups to prevent back migration of OH^- ions from the cathode chamber to the anode chamber. Although highly selective for monovalent cations, these membranes are easily susceptible to scaling in the presence of divalent Ca^{2+} and SO_4^{2-} ions. This scaling results in increased concentration polarization losses and reduced electrolytic efficiencies.

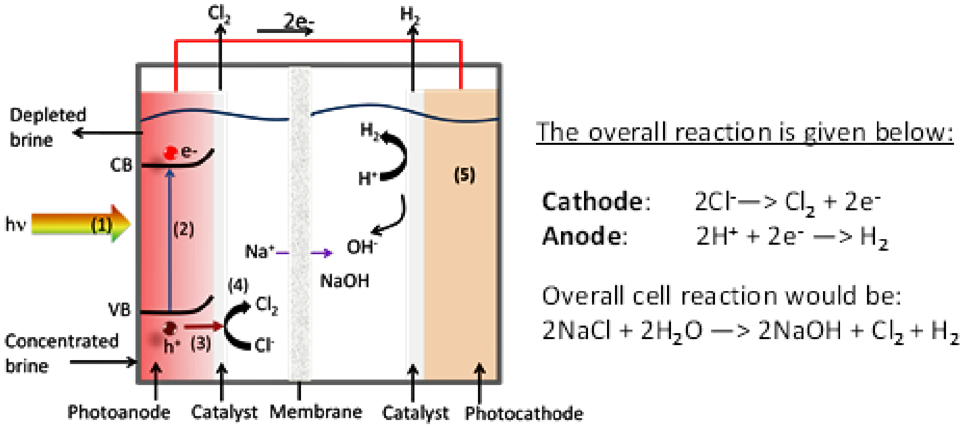

Figure 5.—Schematic of the overall reaction of the proposed photochloralkali process for conversion of ions in brine waste to value-added chemicals.

To overcome scaling challenges, we developed an inorganic, electrically conducting membrane using porous anodic alumina as the growth template. The alumina template was either coated with conducting carbon or metal nanotubes to impart electrical conductivity (more details in Section 3. Results and Discussion). The ion-selectivity on the as-synthesized membranes were imparted simply by controlling the direction of the electric field (Figure 6). Further, the membranes were periodically triggered using a DC voltage source to prevent supersaturation of Ca^{2+} ions and SO_4^{2-} ions near the membrane surface—which results in scaling issues (Bowen et al. 1989 and Jagannadh and Muralidhara 1996). For example, applying a positive voltage to the membrane will result in electrostatic repulsion of Ca^{2+} ions, resulting in it being pushed away from the membrane surface to the bulk layer.

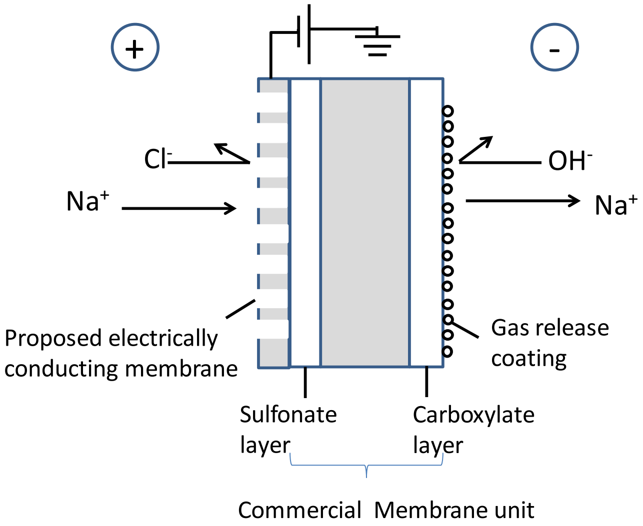

Figure 6.—Side view of the proposed electroactive ion-exchange membrane.

2.3. Project Facility/Physical Apparatus

2.3.1. Source Water

Concentrated brines produced from different source water feeds were tested under simulated solar irradiation using a bench-top unit. Different brines were investigated, including:

- "Ideal" NaCl (NaCl concentration of 1 wt% to 10 wt%)
- "Simulated" NaCl with different concentration of $CaCl_2$, $MgCl_2$, Na_2SO_4 to assess the effect of mono-and divalent cations and anions
- A water sample from the Brackish Groundwater National Desalination Research Facility (BGNDRF) facility—RO concentrate from Well 4.

2.3.2. Material Synthesis and Characterization

For nanomaterials synthesis, chemical vapor deposition, electrodeposition, and anodization tools were utilized. Supporting equipment for the photoelectrochemical research includes a multi-channel multipotentiostat / galvanostat (Bio-Logic), a custom-built solar simulator and a flow-through electrochemical reactor.

2.4. Methods Used/Experiments Done/Analytical Process

2.4.1. Photoelectrodes for H_2 Production (Tin Sulfide/CdS/TiO_2/Pt)

2.4.1.1. Synthesis

“**Chemical bath deposition of tin sulfide**: Fluorine-doped tin oxide (FTO) glass slides were used as a substrate for depositing tin sulfide films. All chemicals were purchased from Sigma-Aldrich, Massachusetts. Prior tin sulfide deposition, the FTO substrates were ultrasonically cleaned in acetone, isopropanol and deionized (DI) water for ten minutes each. To prepare the growth solution for chemical bath deposition, first, 0.1 M $SnCl_2{\cdot}2H_2O$ (purity ≥99.995%) was completely dissolved in 20 milliliters (ml) of acetone. This was followed by addition of 0.75 molar (M) of triethanolamine (TEA) (purity ≥99.0%), 20 ml of commercial ammonium hydroxide (28-31%) and 20 ml of DI water. Enough time for mixing (about 4 minutes) was allowed between the additions of TEA, ammonium hydroxide, and water. The solution was stirred for another 4 to 5 minutes before adding 0.1 M of thioacetamide (purity ≥ 99.0%). DI water was added to make the volume of total growth solution equal to 200 ml. The growth solution was then kept at 85 degrees Celsius (°C) in an oil bath. FTO substrates were then immersed in the solution with their conductive sides facing downward angling 60 degrees to the bottom of the beaker. After the CBD deposition for the required amount of time (0.5 to 2 hours), the substrates were taken out of the growth solution, rinsed with DI water and then left to dry naturally in the air. All samples were annealed in nitrogen for 1 hour at 200 °C before PEC runs.

Chemical bath deposition of cadmium sulfide (CdS): Cadmium sulfide was deposited on tin sulfide films following well-established CBD recipes previously reported (Sun et al. 2012) The solution for CBD growth of CdS included 0.01 M of cadmium sulfate, 0.0125 M of ammonium sulfate, 0.075 M of thiourea, and 0.025 M of potassium iodide in 100 ml DI water. All chemicals were purchased from Sigma-Aldrich. The pH of the chemical bath was adjusted to 11.5 by adding ammonium hydroxide. The CdS growth solution, under mild magnetic stirring, was heated to 80 °C in an oil bath. The CBD-grown tin sulfide films were vertically submerged into the CdS growth solution. After 20 minutes of CBD, the samples were taken out of the solution, rinsed with DI water and dried naturally in the air.

Atomic layer deposition of TiO_2 and Pt deposition: The atomic layer deposition (ALD) of TiO_2 was carried out in an Oxford FlexAL tool at 200 °C using tetrakis(dimethylamino)titanium (TDMAT) and water as precursor and reactant, respectively (Zhou et al. 2010). After ALD deposition, the samples were annealed at 200 °C under a nitrogen atmosphere before e-beam evaporation of platinum. A mass equivalent thickness of 2 nm of Pt was deposited as the hydrogen evolution catalyst for all the samples.

2.4.1.2. Structural Characterization

The morphology of the films was characterized using a field emission scanning electron microscope (Hitachi S-4800) and a field emission transmission electron microscope (JEOL JEM 2100F, FEG). X-ray diffraction (XRD) patterns were acquired with a Philips X'PERT multipurpose diffractometer (MPD), using Cu Ka radiation (1.5405 angstroms [Å]) over a range of $2\theta = 20° - 60°$ at a scan rate of 4° min^{-1}. XPS analysis was carried out using Kratos Axis Ultra x-ray photoelectron spectrometer with concentric hemispherical electron energy analyzers combined with the established delay-line detector (DLD). The incident radiation monochromatic Al $K\alpha$ X-ray (1486.6 electron volts [eV]) at 150 watts (W) (accelerating voltage 15 kilovolts [kV], emission current 10 milliamps [mA]) was projected at a 45° angle to the sample surface, and the photoelectron data was collected at takeoff angle of $\theta = 90°$. The absolute energy scale was calibrated to Cu $2p_{3/2}$ peak binding energy at 932.6eV using sputter-etched 99.9999% pure copper foil. The base pressure in the analysis chamber was maintained at $1.0x10^{-9}$ Torr. Low energy electrons were used for charge compensation to neutralize the sample.

Survey scans were taken at pass energy of 160eV and carried out over 1200eV ~-5eV binding energy range with 1.0eV steps and a dwell time of Two hundred milliseconds (ms). High-resolution scans of Sn 3d, Cd 3d, and S 2p were taken at pass energy of 20eV with 0.1eV steps and a dwell time of 1,000 ms. The spectra analyses were carried out using CasaXPS version 2.3.18PR1.0. A Shirley-type background was routinely used to account for inelastically scattered electrons that contribute to the broad background. Transmission-corrected relative sensitivity factors (RFS) / Kratos library were used for elemental quantification.

The spectra were calibrated using adventitious carbon C 1s peak at 284.8 eV. Dynamic secondary ion mass spectroscopy (DSIMS) was performed with a Cameca IMS 7f-Auto system using an oxygen (O_2 +) primary ion beam at an impact energy of 2 kV. Typical background pressure in the system was $1 \times 10{-}9$ millibars (mbar). The crater size was 175 microns (μm), and secondary ions were monitored from a 63-μm diameter circle in the center to avoid crater-edge effects. Various secondary ion species were monitored, and data were recorded at intervals of approximately 1 nm depth for each element. Depth scales were quantified using a contact profilometer.

2.4.1.3. Photoelectrochemical Characterization

Photoelectrochemical measurements using polysulfide redox couple: PEC measurements for the redox couple of HS^-/S_2^{2-} were carried out in a three-electrode configuration with bare tin sulfide thin films as the working electrode. A 300 W xenon lamp source fitted with AM 1.5 and IR filter was used to simulate sunlight with an intensity of 100 mW/cm^{-2} measured using a thermopile sensor (Newport). All linear sweep voltammetry (LSV) measurements were carried out at a scan rate of 20 mV s^{-1}. For the redox couple of HS^-/S_2^{2-}, the electrolyte composition was 0.1 M Na_2S + 0.1 M S (pH = 9), with saturated calomel electrode (SCE) and Pt wire as reference and counter electrode, respectively.

Photoelectrochemical measurements for hydrogen production: For PEC studies of H_2 production, 0.5 M H_2SO_4 was used as an electrolyte with SCE and Pt wire as a reference and counter electrodes, respectively. The scan rate for the linear sweep voltammetry and the cyclic voltammetry was ten mV s^{-1}. The photoelectrodes were illuminated with simulated AM 1.5 solar spectrum (Newport Xe Arc Lamp Source) equipped with liquid IR filter and a cut-off filter (λ>500 nm). The incident light intensity was measured to be 80 mW cm^{-2}. Photocurrent stability tests were carried out by measuring photocurrents under chopped light illumination at a fixed electrode potential of 0 V vs. RHE. Before linear sweep voltammetry and chronoamperometry measurements, the electrolyte was bubbled continuously with N_2 to remove oxygen—thereby eliminating any erroneous signals arising from oxygen reduction.“ (Cheng W., Mubeen S., et al., 2017)

2.4.2. Photoelectrodes for Cl_2 Production ($BiVO_4$/WO_3):

2.4.2.1. Synthesis

“$BiVO_4$ Synthesis: The bismuth vanadate photoanodes were synthesized following a previously published procedure (Khawaii et al. 2008). The pH of a 50 ml 0.4 M KI solution was adjusted to 1.7 using dilute HNO_3. $BiNO_3$ $5H_2O$ was added to make a 0.04 milliMolar (mM) solution. A 10 ml solution of 0.23 M p-benzoquinone dissolved in anhydrous ethanol was added and stirred for 30 minutes. Before electrodeposition, the FTO was cleaned by ultrasonication in acetone, methanol, and isopropanol and dried with a stream of nitrogen.

Electrodeposition of BiOI on the FTO working electrode was carried out using a VSP-300 Biologic multichannel potentiostat. A Pt coil and saturated Ag/AgCl were used as counter and reference electrodes, respectively. The deposition was conducted by applying a bias of -0.1 volts (V) vs. the reference electrode until One hundred thirty millicoulombs per square centimeter (mC/cm^2) of charge was passed. After rinsing with water, the samples were dried with N_2 and then placed in a muffle furnace. One hundred fifty microliters (µL) of 0.2 M vanadium acetylacetonate dissolved in DMSO was drop-casted on each film. The samples were then annealed at 450 ^{o}C for 2 hours with a temperature ramp of 2 ^{o}C/min. Excess vanadium oxide was removed via gentle stirring in 1M NaOH for 15 minutes.

WO_3 Deposition: Tungsten oxide was electrochemically deposited based on previously published process (Peñate and García-Rodríguez 2012). The WO_3 electrodeposition solution was prepared by dissolving 0.93 grams (g) of tungsten powder in 10 ml of 30 percent peroxide. After dissolution, platinum coils were used to decompose excess peroxide, which was confirmed with peroxide test strips. The stock solution was subsequently diluted to 100 ml using a 65:35 (water: isopropyl alcohol) solution and allowed to age for one week while stored in a fridge. The deposition was carried using a bismuth vanadate working electrode, Pt coil counter electrode, and saturated silver/silver chloride (Ag/AgCl) reference electrode. A bias of -0.5V vs. Ag/AgCl was applied until the desired charge density was passed. The samples were then rinsed with isopropyl alcohol (IPA), then H_2O, and then dried in a muffle furnace at 275 ^{o}C for 10 minutes.

2.4.2.2. Structural Characterization

Structural characterization was carried out using Hitachi S-4800 SEM. Ultraviolet-visible spectrophotometry (UV-Vis) measurements were carried out using a thermos-scientific evolution 300 UV-Vis spectrophotometer.

X-ray photoelectron spectroscopy (XPS) analysis was carried out using a similar protocol as mentioned for SnS-based photocathodes. Survey scans were taken at pass energy of 117.4 eV and carried out over 1200 eV ~-0 eV binding energy range with 0.3 eV steps and a dwell time of 30 ms. High-resolution scans of Bi 4f, V 2p, W 4f, and O 1s were taken at pass energy of 25.3 eV with 0.05 eV steps and a dwell time of 30 ms.

Transmission electron microscopy (TEM) and energy-dispersive x-ray spectroscopy (EDS) analyses were performed using field electron and ion company's (FEI) Titan Themis Z instrument equipped with image-and probe-forming spherical aberration (Cs) corrector. TEM samples were sonicated in ethanol and then dropped onto holey carbon TEM grids for analysis. High-resolution transmission electron microscopy (HRTEM) images were acquired at an accelerating voltage of 300 kV. Each EDS collection was conducted using a four-quadrant FEI Super-X detector.

2.4.2.3. Photoelectrochemical Characterization

The photoelectrochemical measurements were carried out in a two-compartment quartz cell. The $BiVO_4$ WE and Ag/AgCl RE were separated from the Pt coil CE by a glass frit. The $BiVO_4$ was illuminated through the FTO back contact via simulated sunlight from a 300W Xenon arc lamp fitted with an IR and AM 1.5 filter. A Newport 919P-03-10 thermopile detector was used to confirm a final light intensity of 100 mW/cm^2.

J-V plots were constructed by sweeping from the open circuit potential at a rate of 20mV/s. Baseline measurements were performed in 1M sodium sulfite hole scavenger with 0.5 M phosphate buffer with a pH adjusted to 7.4. Chlorine oxidation was carried out in a 4M NaCl solution with its pH adjusted to 1 using hydrochloric acid. Results were plotted in comparison to the reversible hydrogen electrode using Equation 1:

$$V_{RHE} = V_{AgAgcl} + 0.197\ V + 0.059\ V\ pH \qquad (1)$$

Stability tests were conducted by applying a constant bias of 1.419 V vs. RHE (standard redox potential for chlorine evolution).

Product analysis: Each compartment of the quartz cell was purged with helium for 1 hour before taking measurements. Hydrogen and oxygen were measured by extracting 250 microliters (μL) of headspace and injecting it into an SRI 8610C GC with a Mol Sieve5A column equipped with a helium ionization detector. After the experiment, the compartment housing the bismuth vanadate working electrode was gently purged with helium which passed through a potassium iodide trap solution to collect chlorine. This chlorine was quantitatively measured via Iodometric titration with sodium thiosulfate using starch as an indicator." (Rassoolkhani et al., 2018)

2.4.3. Electroactive Ion-Exchange Membranes

2.4.3.1. Synthesis

Overview of synthesis procedure: The general synthesis scheme is initiated by fabricating a porous anodic aluminum oxide (AAO) template of desired thickness by electrochemically anodizing aluminum foil. The AAO template is removed from the aluminum by a selective chemical etching process. Then a thin and uniform polystyrene or polyacrylonitrile (PAN) film is deposited inside AAO using a well-established dip coating technique so as to ensure conformal deposition, good film integrity and thickness uniformity (Zheng et al. 2011). In step 5, hollow carbon nanotubes were synthesized by high-temperature carbonization of polystyrene or PAN (Yang et al. 2013).

Tuning pore diameter and pore density: We tuned by first synthesizing AAO membranes with pore sizes in the range of 10 - 30 nm, followed by controlled tuning of carbon coating thickness both at the surface and inside of the pore walls. The pore diameter and interpore distance of AAO depend on the anodization voltages and the electrolyte and follow a linear relation, as shown in Equations 2 and 3. The pore density, defined as the ratio of the total number of pores occupying a density of 1 square centimeter (cm^2) is given by Equation 4 (Sulka 2008).

$$D_p = k_p U \qquad (2)$$

$$D_{int} = k_{int} U \qquad (3)$$

$$D_{den} = \frac{2\times 10^{14}}{\sqrt{3}\times D_{int}} \qquad (4)$$

where:
D_p is the pore diameter,
D_{int} is the interpore distance
D_{den} is the pore density
U is the anodization potential

2.4.3.2. Structural Characterization

Characterization: The synthesized membranes were characterized structurally using scanning electron microscopy (SEM) and transmission electron microscopy (TEM) to determine structural morphology and SEM-EDX and x-ray photoelectron spectroscopy (XPS) for bulk and surface chemical composition, respectively, of the core-shell electroactive membranes.

Tuning Ion-selectivity: The ability of the membranes to reject ions was primarily explored using potentiostatic approaches (i.e., controlling the ion-selectivity by injecting excess charges into the membrane). For example, excess negative charges can be created at the inner walls by applying a negative potential. Ions with the same charge will get repelled, and counter-ions will flow through." (Mubeen et al. 2017)

2.4.3.3. Synthesis and Characterization of Metallic Electroactive Membranes

The general synthesis scheme is similar to descriptions of schemes in the above sections, except here instead of coating alumina walls with a polymer, metal alloy nanowires were electrodeposited inside the alumina followed by selective etching of a metallic element (details in Section 3. Results and Discussion). Pore diameter and pore density were controlled by tuning the alloy composition and etching time. The membranes were characterized similar to the protocols mentioned above.

2.4.4. Standalone Solar-Powered Lab Scale Demonstration:

Demonstration of a lab-scale stand-alone solar powered unit was completed using triple junction amorphous silicon solar cells coated with appropriate hydrogen evolution and chlorine evolution catalyst. A triple junction Si solar cell was used to generate the necessary photovoltages to run the concentrate management unit using sunlight as the sole energy input.

2.4.5. Technoeconomic Analysis

In this task, we first developed a standardization approach and set of performance and economic assumptions to estimate the total cost of freshwater production due to the integration of the proposed concentrate brine management unit. We modified an open source hydrogen production analysis (H2A) model developed by the Department of Energy for performing our cost calculations. Steps for this analysis were:

1. Defined basic process information (feed water sources, energy inputs, size of plant, products, and co-products produced, etc.). We included different sources of brackish water as a feed stream to produce 1,000 cubic meters per day of clean water under the conditions necessary for drinking supply.

2. Defined process flowsheets and stream summary (flowrate, temperature, pressure, the composition of each stream)
3. Defined technology performance assumptions (e.g., process efficiency, fresh water produced, product state and conditions)
4. Defined economic assumptions (e.g., after-tax internal rate of return, depreciation schedule, plant lifetime, income tax rate, capacity factor).
5. Reference year dollars: 2018
6. After tax, internal rate of return: 10%
7. Inflation rate: 1.8%
8. Effective total tax rate: 38.9%
9. Depreciation period and schedule: Modified Accelerated Cost Recovery System (MACRS)
10. Plant lifetime: 20 years
11. Decommissioning costs are assumed equal to salvage value
12. Developed a standardized spreadsheet to calculate discounted cash flow
13. Developed a standardized format to compare results (e.g., water treatment cost, hydrogen selling price, operating efficiency, feedstock consumption, savings in pre-treatment chemical usage due to the production of Cl_2 and NaOH)
14. Performed sensitivity analysis for different parameters (e.g., feedstock cost, pre-treatment cost, product and by-product selling price, capital cost, operating costs, internal rate of return, conversion efficiencies)

3. Results and Discussion

3.1. Task 1.0. Fabricate, Study and Test Photoelectrodes for Concentrated Brine Treatment

3.1.1. H_2 Production Photocathodes (Tin Sulfide-based Photoelectrodes)

In this study, we analyzed PEC properties of crystalline nanoplatelet tin sulfide photocathodes fabricated using low-cost, solution processable technique for solar H_2 production. First, using a regenerative PEC system (no net chemical change), we demonstrated that the tin sulfide nanoplatelet thin films can serve as efficient photocathodes with a maximum photocurrent density of 12 mA cm^{-2}. We then developed a simplistic strategy to fabricate type-II heterojunction H_2 producing photocathodes, consisting of p-tin sulfide/n-CdS/n-TiO_2/Pt. In this task, we demonstrated H_2 production at a current density of 2.4 mA cm^{-2} at 0 V vs. RHE in acidic media with the highest reported incident photon-to-electron conversion efficiency (IPCE) for these materials to date.

The tin sulfide thin films were synthesized on fluorine doped tin oxide (FTO) coated glass using a modified chemical bath deposition (CBD) method. Detailed accounts of the synthetic method are given Section 2. Technical Approach and Methods. Figure 7a and Figure 7b show top and cross-sectional scanning electron microscopy (SEM) images of tin sulfide films deposited on the FTO substrate. The films produced using chemical bath deposition showed nanoplatelet morphology with individual platelets of thickness 12.3±1.0 nm (Figure 7a, inset) and a total height of approximately 600 nm. The nanoplatelet morphology is an effective structure for light absorption and carrier extraction, as the nanoplatelets collect carriers orthogonally to the direction of the incident light. Areas over 5.0 cm^2 were frequently produced with no delamination of films observed in any of the samples.

Transmission electron microscopy (TEM) (Figure 7c) and X-ray diffraction (XRD) measurements (Figure 7d) revealed highly crystalline orthorhombic structured tin mono-sulfide films with strong <111> orientation. Band gap and direct/indirect transitions of the tin sulfide films were determined using the Tauc equation as shown in Equation 5:

$$(\alpha h\nu)^n = k(h\nu - E_g) \qquad (5)$$

Where:
α is the measured optical absorption coefficient
$h\nu$ is the photon energy
E_g is the band gap
k is the proportionality constant

A linearity of the plot $(\alpha h\nu)^n$ vs. $h\nu$ was obtained for n = ½, an indicative of indirect transition with x-axis intercept of 1.1 eV, indicating the band gap of the synthesized films (Figure 7e).

To determine the conductivity type and carrier concentration of tin sulfide films, Mott-Schottky plots ($1/C^2$ vs. E) were constructed in 0.1 M Na_2S + 0.1 M S (pH 9) (Figure 7f). C is the differential capacitance, and E is the applied potential with respect to reversible hydrogen electrode (RHE). The tin sulfide films showed a region of ~300 millivolts (mV) where $1/C^2$ linearly increased with decreasing potential under reverse bias conditions, indicating p-type behavior. The p-type behavior and E_{fb} obtained from Mott-Schottky measurements matched with previously reported theoretical estimations for tin sulfide.

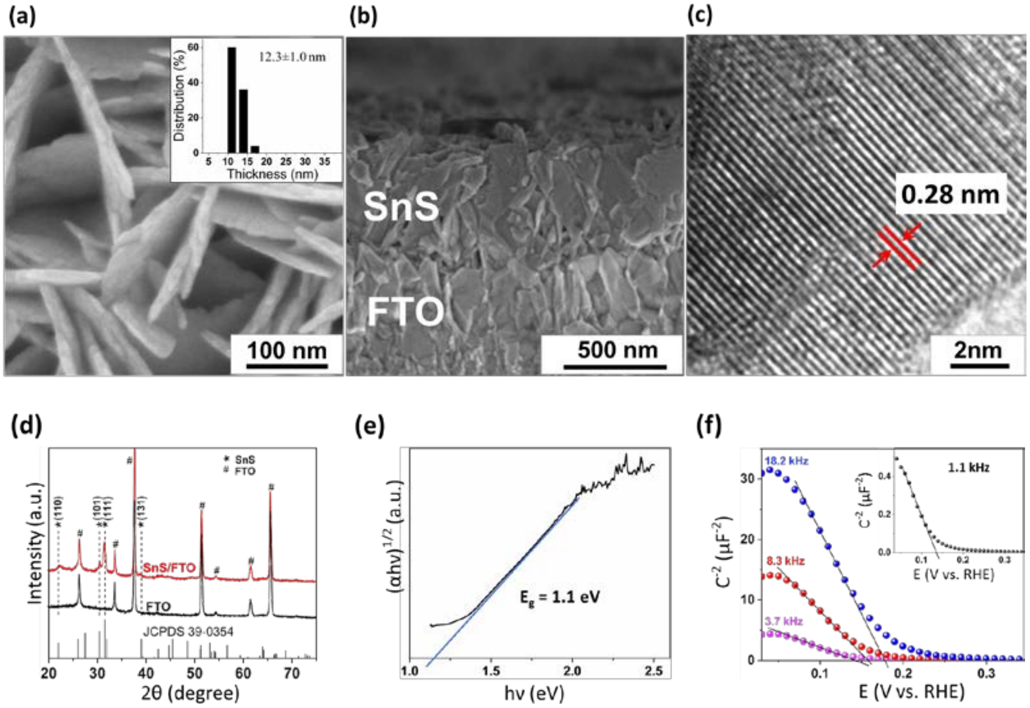

Figure 7.—Top-view (a) and cross-sectional (b) scanning electron microscopy (SEM) images of tin sulfide film deposited on FTO glass substrate. Inset of Figure 1a shows the thickness distribution of tin sulfide nanoplatelets. (c) Lattice-resolved high-resolution transmission electron microscopy (TEM) image of a tin sulfide nanoplatelet showing d-spacing of 0.28 nm corresponding to tin sulfide (111). (d) X-ray diffraction spectrum (XRD) of FTO glass, tin sulfide film deposited on FTO substrate with JCPDS card (No. 39-0354) of Herzenbergite tin sulfide. # marks and * marks indicate peaks of FTO and tin sulfide, respectively. (e) Tauc analysis of optical absorption spectra showing an indirect band gap of 1.1 eV for tin sulfide. (f) Mott-Schottky plots measured for tin sulfide film in 0.1 M Na_2S + 0.1 M S (pH 9) for different frequencies: 1.1 kilohertz (kHz) (black trace, inset), 3.7 kHz (pink trace), 8.3 kHz (red trace) and 18.2 kHz (blue trace).

The PEC properties of tin sulfide photocathode were first tested in the presence of regenerative polysulfide redox couple (S_2^{2-}/HS^-), shown in Figure 8. In a PEC system with the regenerative redox couple, the semiconductor electrode and counter electrode perform the same electrochemical reaction—but in the opposite directions. Thus, the photon energy is converted into electrical energy with no net chemical change to the system. The redox couple most often serves to stabilize the semiconductor from PEC corrosion and provides a fast and convenient way to evaluate the structure-activity relationship of the semiconductor electrode without the complexity of surface passivation. The photocurrents were measured using a three-electrode PEC cell with Pt wire as the counter electrode and a saturated calomel electrode as the reference electrode. A light fluence of 100 mW/cm^{-2} obtained from 300 W xenon lamp fitted with appropriate atmospheric mass (AM 1.5) and infrared (IR) filters were used for all regenerative

PEC runs (see Section 2.4.1 for details). A chopped illumination was used for the measurements so that the dark and photocurrents could be monitored simultaneously.

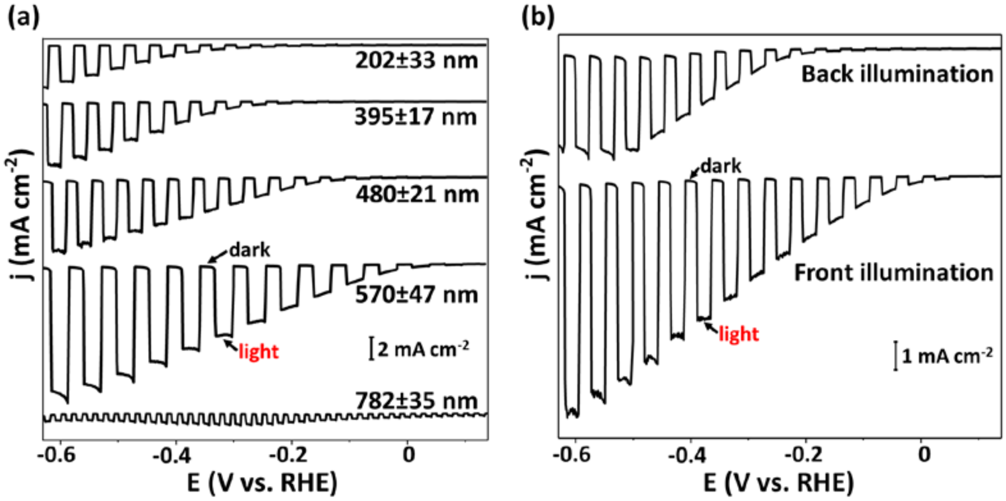

Figure 8.—PEC characterization of tin sulfide films in 0.1 M Na_2S + 0.1 M S (pH 9) under chopped simulated sunlight (AM 1.5). (a) Current density-potential (j-E) characteristics of the tin sulfide films synthesized with different thicknesses (202±33 nm, 395±17 nm, 480±21 nm, 573±47 nm, 782±35 nm) illuminated from the front side. (b) j-E plots of tin sulfide films with a thickness of ~600 nm under back illumination and front illumination.

Figure 8a shows typical current-potential curves obtained in S_2^{2-}/HS^- electrolyte. Negligible cathodic currents were observed for p-tin sulfide in the dark for all potential ranges, as expected for a p-type semiconductor with a low density of electrons (minority carriers) at the surface. Under illumination, the cathodic currents increased substantially since electrons from the valence band were promoted by the absorbed light into the conduction band and were available for reduction reactions. The measured photocurrents increased with increasing thickness of the deposited film (Figure 8a), which was controlled by changing the chemical bath deposition time. Tin sulfide films about 600 nm thick were enough to absorb all incident light with wavelengths < 1,100 nm, yielding a photocurrent density of 12 mA cm^{-2} under 100 mW cm^{-2} front illumination (AM 1.5 solar spectrum). This is the highest reported photocurrent to date for tin sulfide-based photocathodes in the presence of aqueous redox electrolytes. Thicknesses beyond 600 nm (~750 nm) yielded low photocurrent density. This could be due to majority carrier transport limitation due to the increased distance of the majority carriers to transport through the film. The photocurrent density was lower when the sample was illuminated from the back than from the front (Figure 8b). The decrease in the cathodic photocurrent under back illumination can be attributed to minority carrier recombination as the minority carriers that are generated near the back contact are further from the semiconductor-electrolyte interface.

The optimized tin sulfide photocathodes were then tested for PEC H_2 production in a nitrogen purged 0.5M H_2SO_4, which was the electrolyte used for all H_2 production experiments. For all experiments, a platinum (Pt) wire served as the counter electrode, and a saturated calomel electrode served as the reference electrode (see Section 2.4 for details). Nitrogen was purged to remove oxygen and to eliminate the possibility of the oxygen reduction reaction.

Figure 9a shows the chopped photocurrent density transient (j-t plot) at 0 V vs. RHE ($E_{RHE} = E_{SCE} + 0.241\ V + 0.059*pH$) for bare p-tin sulfide coated with 2 nm electron beam deposited Pt nanoparticles. The Pt nanoparticles served as the catalyst for H_2 evolution. Under AM 1.5 illumination, bare tin sulfide films with Pt catalyst produced an initial cathodic photocurrent density of 2.9 mA cm^{-2}. However, the photocurrents decreased substantially over time, indicating chemical and photoelectrochemical degradation of tin sulfide films in the acidic environment of the electrochemical cell. Discoloration of the films could be seen visibly, and the deposit completely disappeared after 30 minutes.

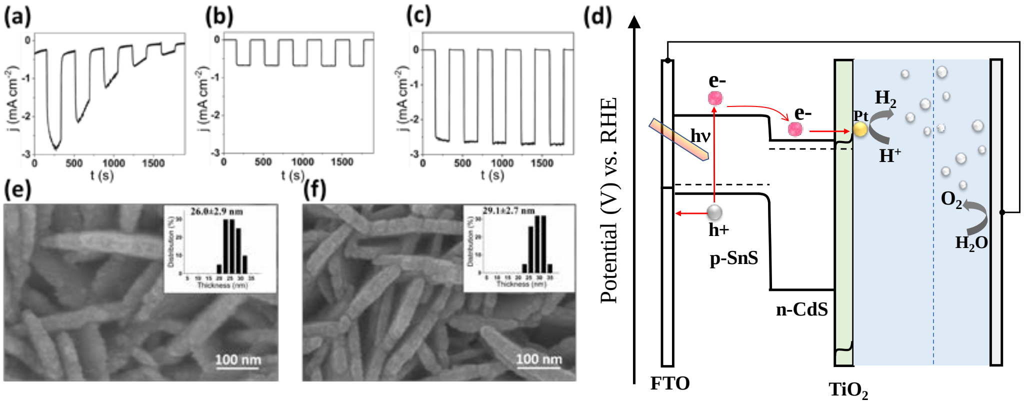

Figure 9.—Current density-time (j-t) characteristics of (a) Tin sulfide/Pt, (b) Tin sulfide/TiO_2/Pt, and (c) P-tin sulfide/n-CdS/n-TiO_2/Pt in 0.5 M H_2SO_4 under chopped simulated sunlight. (d) The energy band diagram of p-tin sulfide/n-CdS/n-TiO_2/Pt for PEC water splitting. Top-view SEM images of (e) Tin sulfide/CdS and (f) Tin sulfide/CdS/TiO_2 deposited on FTO substrate with corresponding thickness histograms shown in the inset.

To protect the tin sulfide films from degradation, 2 nm mass equivalent thick TiO_2 films were deposited on top of tin sulfide using atomic layer deposition (ALD). Thin conformal layers of TiO_2 have been shown to effectively protect underlying semiconductors (such as Cu_2O and Si) from photocorrosion while serving as an effective electron filter due to its large valence band offset. The number of cycles to deposit 2 nm TiO_2 film was obtained from the pre-calibrated ellipsometry data. Chopped photocurrent density transient from the resulting tin sulfide/TiO_2 films with 2 nm electron beam deposited Pt nanoparticles is shown in Figure 9b. Stable photocurrent densities were obtained after adding a TiO_2 layer with a maximum value of 0.6 mA cm^{-2} for the champion device. A buffer layer of CdS between tin sulfide and TiO_2 layer was required to increase the photocurrent density to 2.4 mA/cm^2 (Figure 9c).

Figure 9e and Figure 9f show top view SEM images of tin sulfide/CdS on and tin sulfide/CdS/TiO_2 films with inset showing a histogram of platelet thickness. Adding a CdS layer increased the individual platelet thickness from 12.3±1.0 nm to 26.0±2.9 nm, and a subsequent addtion of a TiO_2 layer increased this thickness to 29.1±2.7 nm. X-ray photoelectron spectroscopy and depth profiling using secondary ion mass spectrometry (SIMS) were used to confirm the chemical composition and heterojunction nature of the films.

Figure 10a shows typical photocurrent density (j)-potential (E) curves for hydrogen production from p-tin sulfide/n-CdS/n-TiO_2/Pt films and p-tin sulfide/Pt films on FTO substrate illuminated with simulated visible solar spectrum (>500 nm and light intensity 80 mW cm^{-2}). Wavelengths greater than 500 nm were chosen for these measurements to eliminate any photocurrents originating from underlying CdS (E_g = ~2.5 eV) and TiO_2 (E_g = ~3.2 eV) layer. When we varied the applied voltage, the p-tin sulfide/n-CdS/n-TiO_2/Pt photocathodes showed a significant enhancement in photoelectrochemical activity with the onset of photocurrents beginning at 0.3 V vs. RHE (a maximum open circuit voltage of ~0.45 V is expected based on the Fermi level difference between p-n tin sulfide/CdS). At 0 V vs. RHE, a photocurrent density of 2.4 mA cm^{-2} was obtained with no evidence of material degradation over the experimental duration. This is the highest photocurrent achieved to date with p-tin sulfide as light absorber material for H_2 production. We stress that no sacrificial reagent was used for H_2 production.

To evaluate electrode stability and the reaction products, gas chromatography (GC) was employed to quantify the amount of H_2 produced. We continued the photoelectrochemical experiment for over 6,000 seconds at 0 V vs. RHE under visible light illumination (λ>500 nm) for p-tin sulfide/n-CdS/n-TiO_2/Pt photocathodes. Before the experiment, the solution was purged with nitrogen to eliminate currents due to oxygen reduction reaction. The evolved H_2 product as measured by GC (blue squares) and the amount of estimated H_2 for 100% Faradaic efficiency (blue triangles) is shown in Figure 10b. We were able to obtain a 90% Faradaic efficiency after two hours. We believe that the 10% loss in Faradaic efficiency is due to experimental error and not due to the photocorrosion of the samples. To further understand the carrier transport process, incident photon-to-electron conversion efficiency (IPCE) and internal quantum efficiency (IQE) measurements were carried out on p-tin sulfide/n-CdS/n-TiO_2/Pt films (Figure 10 [c - e]). The absorptance of the heterojunction photocathode (Figure 10c) was measured using an integrating sphere, which shows the band-edge absorption onset at approximately 1,100 nm.

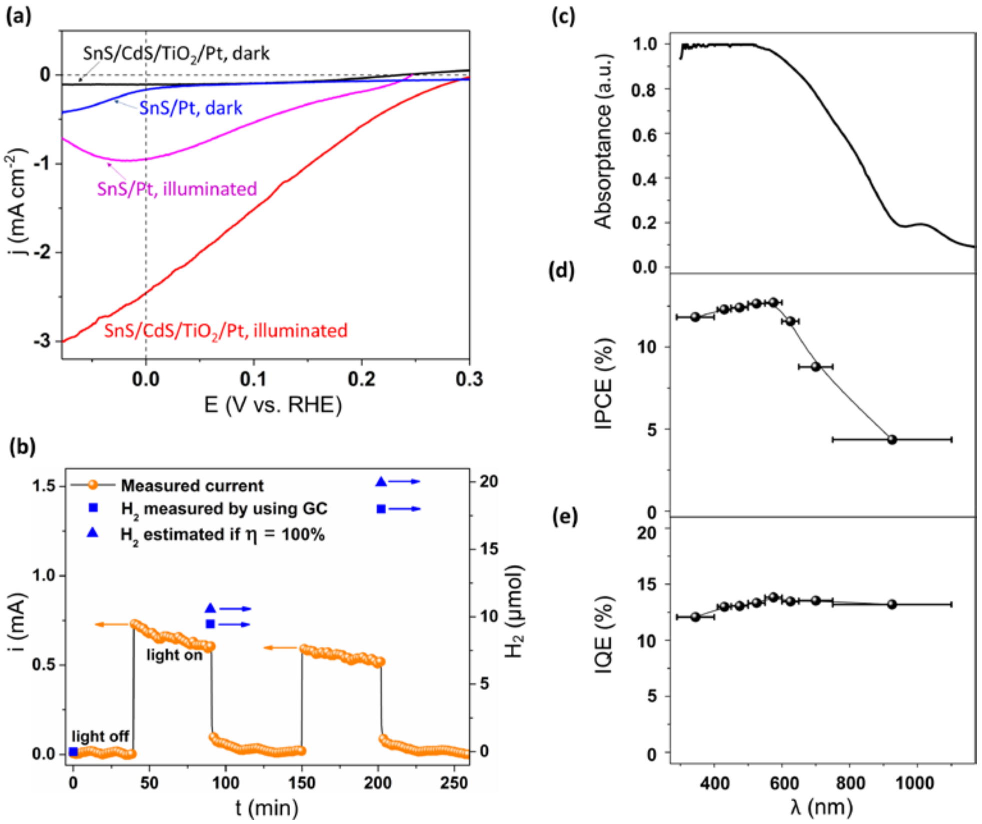

Figure 10.—a) J-E characteristics of p-tin sulfide/n-CdS/n-TiO_2/Pt and p-tin sulfide/Pt electrode in 0.5 M H_2SO_4 solution in dark and under simulated visible sunlight (>500 nm, 80 mW cm^{-2}, red line). (b) Faradaic efficiency measurement for hydrogen production through current-time characteristic (orange sphere) of the heterojunction photocathode in 0.5 M H_2SO_4, illuminated by simulated visible sunlight (>500 nm, 80 mW cm^{-2}). The electrode area was 0.23 cm^2. The amount of H_2 measured by GC (blue square) and the estimated amount of H_2 if Faradaic efficiency were 100% (blue triangle) is also shown. (c) The absorption spectrum of p-tin sulfide/n-CdS/n-TiO_2/Pt film. (d) The incident photon-to-current efficiency (IPCE). (e) Internal quantum efficiency (IQE) of p-tin sulfide/n-CdS/n-TiO_2/Pt photocathode measured under simulated sunlight at 0 V vs. RHE in 0.5 M H_2SO_4.

The IPCE spectrum of p-tin sulfide/n-CdS/n-TiO_2/Pt film in Figure 10d follows the distinct excitonic features of the absorption spectrum of p-tin sulfide covered by n-CdS and n-TiO_2, with the IPCE reaching a plateau at 12.7% near 575 nm. The identical trend between the photoelectrochemical action spectrum and the absorption spectrum of the device is strong evidence that tin sulfide dominates the initiating photo-processes. Finally, the photocurrents produced are mainly determined by the photon capture efficiency, and by the IQE, defined as the number of photo excited carriers in the semiconductor contributing to photocurrent per absorbed photon (Figure 10e). The IQE was determined by scaling IPCE by the fraction of incident photons absorbed by the photocathode unit at a given wavelength. For p-tin sulfide/n-CdS/n-TiO_2/Pt devices, the IQE remained constant at about 13 percent across the entire visible wavelength range. (Cheng et al. 2017).

3.1.2. Cl_2 Production photocathodes ($BiVO_4$-based Photoelectrodes)

We carried chloride oxidation in acidic pH (pH 1) using earth-abundant nanoporous bismuth vanadate ($BiVO_4$) as the light absorber and using electrons provided from the oxidation step to generate hydrogen at the dark cathode. $BiVO_4$ has recently emerged as a promising low-cost photoanode for solar water oxidation due to its favorable band gap (E_g=2.4 eV) and conduction band (CB) edge location (0.1V vs. Reversible Hydrogen Electrode [V_{RHE}]). While $BiVO_4$ is chemically stable in neutral or slightly basic pH conditions, $BiVO_4$ should be stabilized in pH < 3 solution for chloride oxidation to obtain high chlorine production yields. This is because, at neutral or slightly basic pH, the chlorine decomposes to hypochlorous acid, which then subsequently decomposes to O_2 (Equations 6 and 7), resulting in low Faradaic efficiency for chlorine production.

$$Cl_2 + H_2O \rightarrow HClO + Cl^- + H^+ \qquad (6)$$

$$HClO \rightarrow H^+ + Cl^- + \frac{1}{2}O_2 \qquad (7)$$

We addressed the issue of $BiVO_4$ instability in acidic pH environment by conformally depositing amorphous tungsten oxide (WO_3) films on top of nanoporous crystalline $BiVO_4$ films using electrodeposition. Amorphous WO_3 was selected as stabilization element because of its:

i) The large band gap (>3 eV; thereby transmitting most of the incident light to $BiVO_4$)

ii) Good chemical and electrochemical stability under acidic conditions

iii) Selective electrocatalytic activity for Cl^- oxidation over H_2O oxidation

iv) Ability to transfer holes through gap states in its band structure

We found that a WO_3 film 20 nm thick was enough to prevent $BiVO_4$ corrosion while being thin enough to transmit most of the incident light to $BiVO_4$. The best-performing $BiVO_4/WO_3$ photoelectrode assemblies achieved a limiting photocurrent density of 2.5mA/cm^2 and operated sustainably for more than three hours with Faradaic efficiencies of 85% for Cl^- oxidation—the highest reported so far for this material.

Details of the fabrication of $BiVO_4/WO_3$ photoanodes for solar-driven chloride oxidation are given in Section 2. Technical Approach and Methods. Briefly, the $BiVO_4/WO_3$ nanostructured films were deposited on conductive fluorine-doped tin oxide (FTO) coated glass substrate using a two-step process. The first step is the fabrication of crystalline $BiVO_4$ light absorber unit following previously reported methods, where electrodeposited bismuth oxyiodide (BiOI) is used as a precursor to form $BiVO_4$.

Figure 11a and Figure 11c show a top view and cross-sectional scanning electron microscopy (SEM) images of the bare $BiVO_4$ electrode. The SEM images showed a nanoporous architecture for $BiVO_4$ with interconnected particles approximately 90 nm in diameter. A nanoporous architecture with minority carrier diffusion lengths less than 100 nm (as determined by the particle diameter) has been shown to enhance charge separation efficiency while providing a large contact surface area at the $BiVO_4$/electrolyte interface. The WO_3 layer (~20 nm thick) was then subsequently electrodeposited on $BiVO_4$ (Figure 11b) using a peroxytungstic acid solution.

Based on microscopy images (Figure 11d), conformal deposition of WO_3 on the $BiVO_4$ electrode was observed down to the base of the particle while the nanoporous architecture was still intact, preserving the ability to efficiently extract carriers. The thickness of the WO_3 layers can be tuned by adjusting the charge passed during electrodeposition. The optimum thickness was probed by comparing their photoelectrochemical behavior. Under the optimized condition, that is at 100 mC/cm^2 deposition charge density at -0.5 V vs. silver/silver chloride electrode; the WO_3 thickness was approximately 20 nm. As shown in this section later, a 20 nm thick WO_3 film was enough to stabilize $BiVO_4$ in acidic pH conditions while transmitting most of the incident light to $BiVO_4$. The overall thickness of the $BiVO_4/WO_3$ films as measured by the cross-sectional SEM images was about 600 nm (Figure 11c and Figure 11d).

The nanostructured $BiVO_4/WO_3$ films were further characterized using high-resolution transmission electron microscopy (HRTEM), energy-dispersive x-ray spectroscopy (EDS) and x-ray photoelectron spectroscopy (XPS). Figure 11e and Figure 11f show HRTEM images and fast Fourier transform (FFT) patterns of both bare $BiVO_4$ particle and $BiVO_4$ coated with WO_3. Low-magnification images are provided in the supplementary information.

The HRTEM image revealed a crystalline structure for as-synthesized pristine $BiVO_4$ (Figure 11e) with a lattice spacing of 0.307 nm, corresponding to the (112) Crystallographic planes of $BiVO_4$ (JCPDS file no. 14-0688). TEM images of the coated samples (Figure 11f) showed a clear interface between the $BiVO_4$ core and WO_3 shell with WO_3 film coated along the surface of the $BiVO_4$ particle with a uniform thickness of 20 nm. The FFT pattern indicated that the deposited WO_3 film was amorphous in nature (Figure 11f inset). EDS elemental mapping in Figure 11g revealed the compositional variation of the $BiVO_4/WO_3$ particle. The W signal was recorded from the entire area, supporting the conformal coating geometry. Strong Bi and V signals were obtained from the center region, further indicating the existence of the core-shell architecture of the $BiVO_4/WO_3$ particle. No W signal was detected from the bare $BiVO_4$ films.

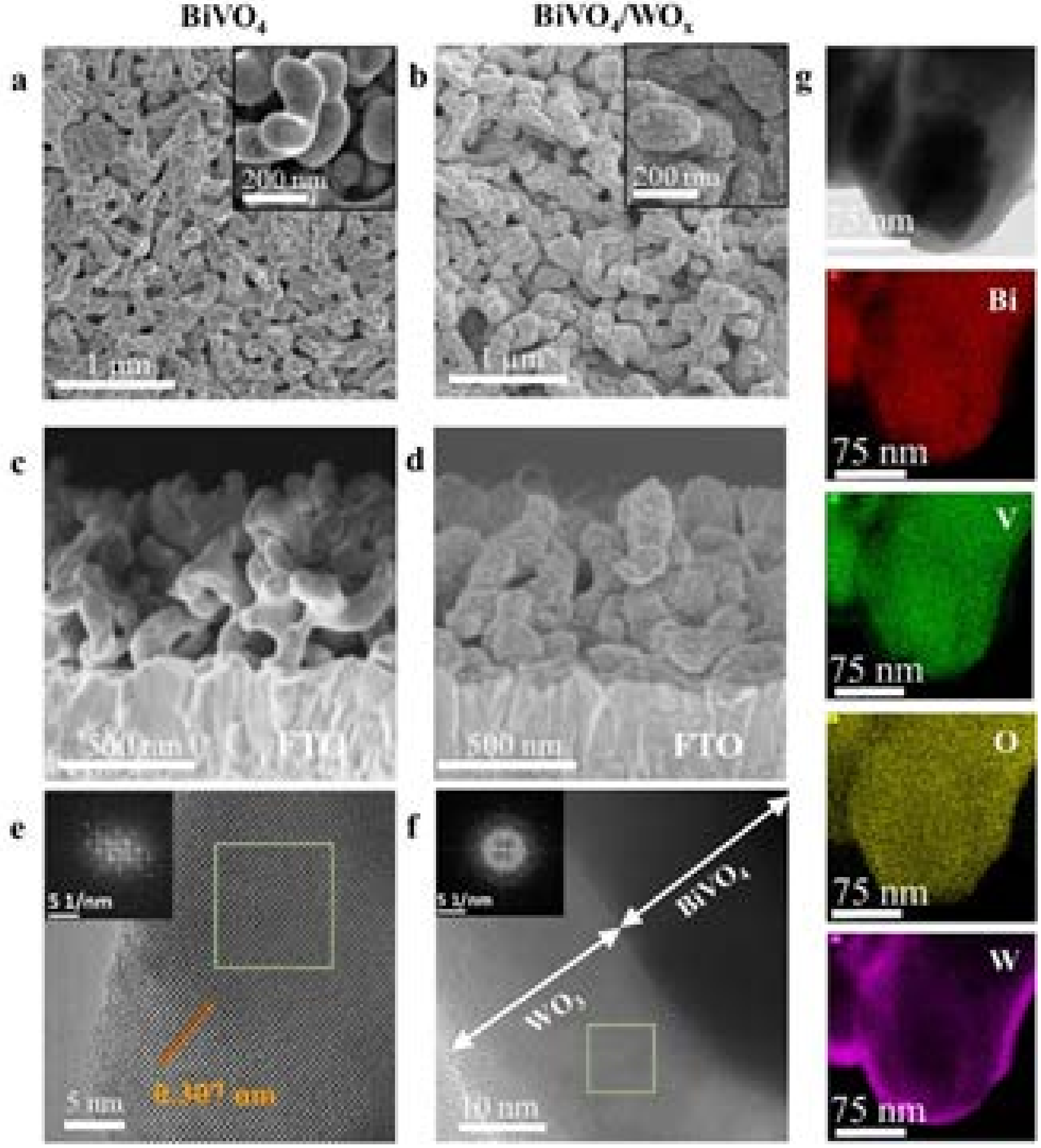

Figure 11.—Physical characterization of $BiVO_4$ and $BiVO_4/WO_3$. Left column, the bare $BiVO_4$ electrode. Right column, the $BiVO_4$ electrode coated with 20 nm thick WO_3. (a), (b) Top view and (c), (d) cross-sectional view SEM images. (e), (f) High-resolution TEM images with inset showing FFT pattern. (g) EDS elemental mapping of the core-shell $BiVO_4/WO_3$ structure.

The PEC properties of the $BiVO_4/WO_3$ photoanodes were characterized in a three-electrode configuration: $BiVO_4/WO_3$ as working electrode, saturated calomel electrode (SCE) as a reference electrode and Pt counter electrode separated using a glass frit. Photo-electro-oxidation of chloride ions using $BiVO_4/WO_3$ photoanode assembly can be explained conceptually by referring to Figure 12a. Upon illumination, photogenerated holes generated in $BiVO_4$ are initially carried away to the surface through amorphous WO_3 films where it oxidizes chloride ions to chlorine. The electrons provided from the oxidation step are transferred through an external circuit to a dark Pt cathode for hydrogen production.

To confirm that the amorphous WO_3 layer does not interfere with the photogenerated carrier transport properties of underlying $BiVO_4$ films, we first investigated the PEC performance of $BiVO_4/WO_3$ photoanode in a phosphate buffer solution with sodium sulfite as the hole scavenger. Prior studies have shown that sulfite oxidation acts kinetically and thermodynamically favorably on $BiVO_4$ electrodes and can be used as a benchmark electrolyte to decouple charge separation efficiency from kinetic losses. Figure 12b shows the typical photocurrent densities obtained for sulfite oxidation as a function of the applied potential under one sun illumination (AM 1.5G; 100 mW/cm^2). All potentials are referenced to reversible hydrogen electrode [V_{RHE}; $V_{RHE} = V_{SCE} + 0.244\ V + 0.059\ pH$] and all PEC results shown here are average values obtained from three samples. An average photocurrent density of 3mA/cm^2 was achieved for $BiVO_4/WO_3$ films at 1.2 V_{RHE}. Photocurrent densities of $BiVO_4/WO_3$ were within ±0.1 mA/cm^2 (±3%) compared to the bare $BiVO_4$ electrode surface (Figure 12b, green trace) indicating that the amorphous WO_3 prepared via electrodeposition technique functions efficiently as a hole transport layer with minimal resistive losses.

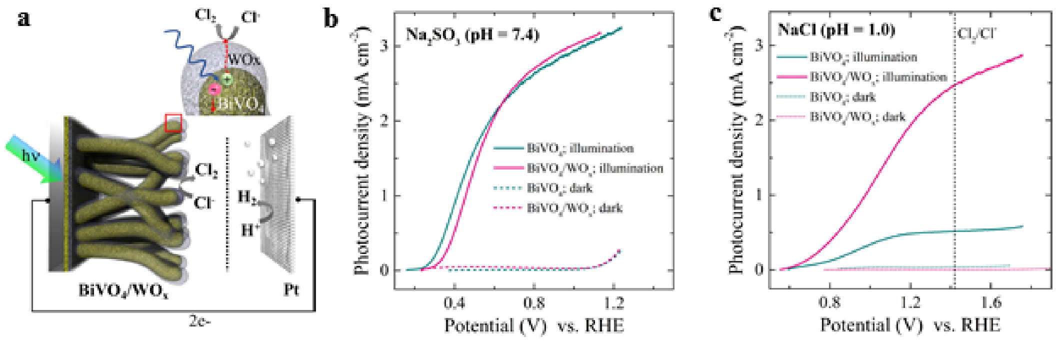

Figure 12.—PEC performance of $BiVO_4$ and $BiVO_4/WO_3$. (a) Schematic showing charge transfer process during the chlorine evolution reaction. Current density - potential (V_{RHE}) plots of $BiVO_4$ and $BiVO_4/WO_3$ coated samples in (b) sodium sulfite hole scavenger solution and (c) in 4M NaCl pH one solution.

The PEC performance of $BiVO_4/WO_3$ films for chloride oxidation was characterized in 4M NaCl solution with pH adjusted to 1 using HCl. No hole scavenger was used for these studies. Figure 12c shows photocurrent density–potential plots for bare $BiVO_4$ and $BiVO_4/WO_3$ photoanodes. All plots are an average of three different samples, and the depicted data are from the 10th linear sweep voltammetric cycle. Each cycle was scanned at a rate of 20 millivolts per second (mV/s), followed by a rest period of 30 seconds.

In the absence of light, negligible anodic current densities ($i < 10$ microamps per square centimeter [µA/cm^2]) were observed for bare $BiVO_4$, and $BiVO_4/WO_3$ samples (Figure 12c, dashed lines). Upon illumination of the substrate, the $BiVO_4/WO_3$ photoanode assembly showed a limiting photocurrent density of 2.8 mA/cm^2 at 1.6V_{RHE}. The limiting photocurrent densities obtained were only slightly lower (≤ 0.2 mA/cm^2) than those observed for the same electrodes in contact with the sulfite solution. This density rate indicates that the chloride oxidation could be carried out efficiently using holes transported to the surface of the amorphous WO_3 layer without the need for an additional catalyst. The onset potential (i.e., the potential at which anodic photocurrent density reaches 20µA/cm^2) was 0.67 V_{RHE} for the $BiVO_4/WO_3$ sample. This onset potential resulted in an estimated photovoltage of 0.75 V after subtracting the thermodynamic potential requirement for chlorine production (1.42 V_{RHE}). For the bare $BiVO_4$ sample, the photocurrents decreased with cycle number with the 10th cycle showing a maximum photocurrent density of 0.75 mA/cm @1.6 V_{RHE}.

The durability of the photoanodes for chloride oxidation was assessed by measuring the photocurrent density as a function of time at a constant external bias of 1.42 V_{RHE} (Figure 13a). The bare $BiVO_4$ samples failed rapidly under illumination, with the visible deterioration of the entire $BiVO_4$ films observed within 15 minutes.

Prior studies have shown that $BiVO_4$ when operated in chloride electrolytes below pH 3, oxidizes to BiOCl with the dissolution of vanadium resulting in material degradation. We found that, on the contrary, $BiVO_4$ samples with WO_3 layer as thin as 20 nm exhibited enhanced stability—maintaining more than 95 percent of initial photocurrent density after three hours of continuous illumination (the duration of these stability tests). Analysis of the $BiVO_4/WO_3$ electrodes post-PEC operation by HRTEM-EDS revealed that the $BiVO_4$ core layer was intact after PEC operation, with the W signal was present throughout the solution and was more pronounced at the edge of the particles (Figure 13b).

Furthermore, no change in the chemical environment of the WO_3 layer was observed after operation using XPS for observations (Figure 13c). To obtain chemical information about the underlying $BiVO_4$ layer post-operation, the WO_3 layer after PEC operation was removed by soaking it in sodium hydroxide solution for 15 minutes. Within this time frame, the NaOH only etches the WO_3 layer without affecting the underlying $BiVO_4$. Core level XPS scans of the Bi 4f and V 2p scans showed peaks identical to that of the bare $BiVO_4$ electrode (Figure 13c). The above results unequivocally demonstrate that the electrodeposited amorphous WO_3 layer could offer a simple and scalable route to protect the underlying nanostructured $BiVO_4$ when operated in acidic media, while still allowing for efficient transport of holes between the solution and the $BiVO_4$ electrode. After two hours of constant potential (1.42 V_{RHE}) PEC runs, the collected products were analyzed to determine the Faradaic efficiency of the process (Figure 14).

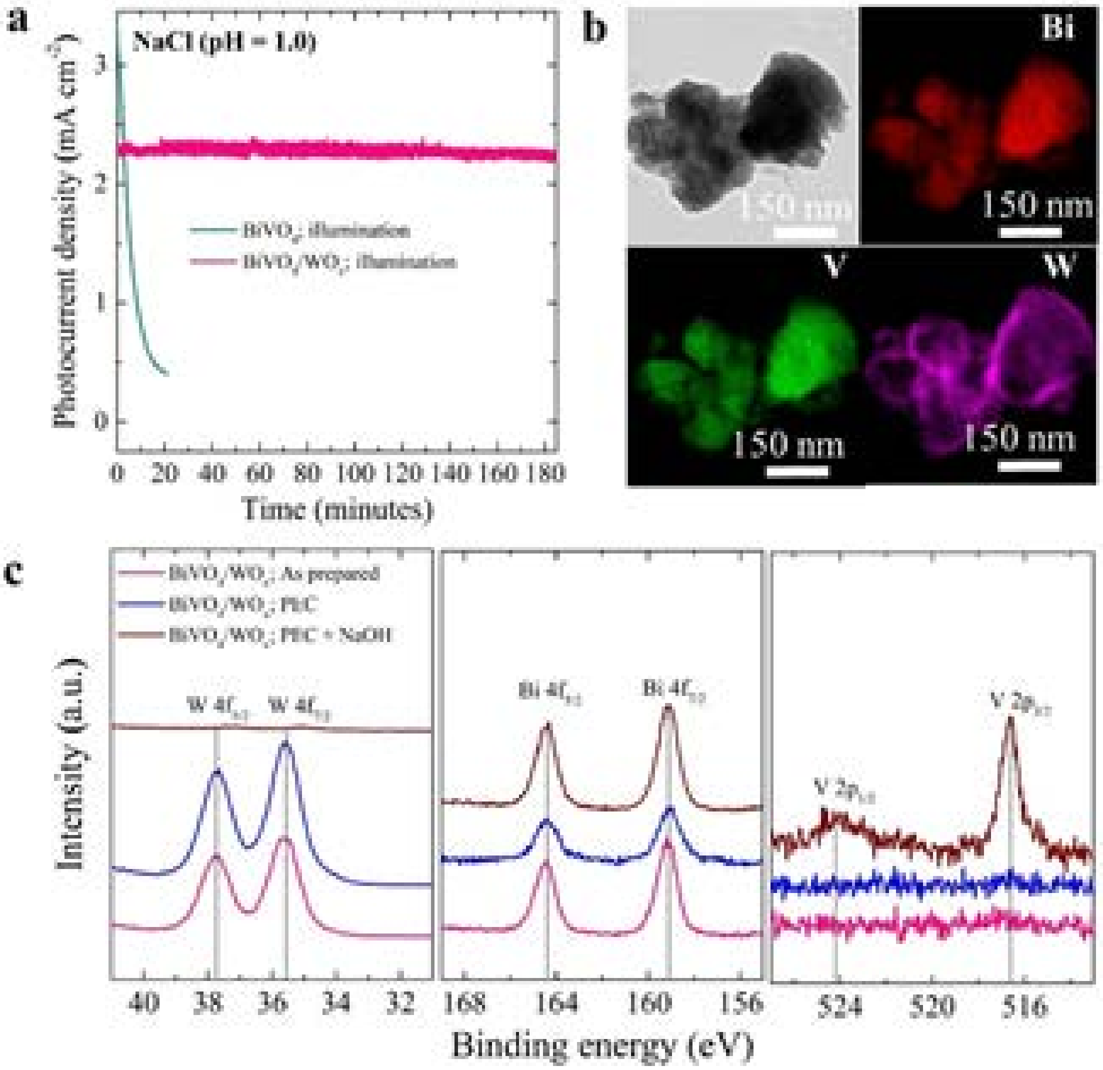

Figure 13.—PEC stability of $BiVO_4$ and $BiVO_4/WO_3$. (a) Photocurrent density - time transient plot for $BiVO_4$ and $BiVO_4/WO_3$ sample for chloride oxidation at 1.42 V_{RHE} under one sun illumination. (b) EDS elemental mapping of the $BiVO_4/WO_3$ structure post operation. (c) Core level XPS scans of W, Bi, and V as prepared (pink trace) and after PEC operation (blue trace). Core level scans of W, Bi, and V after removal of WO_3 layer post operation is also shown (brown trace).

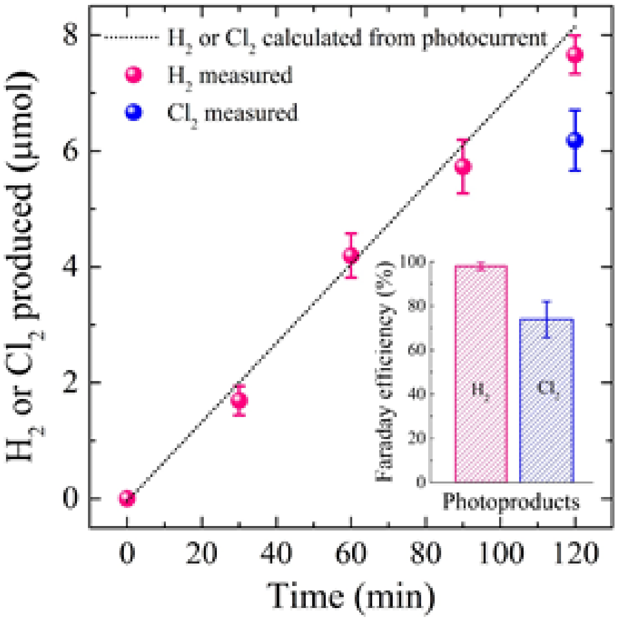

Figure 14.—Faradaic efficiency. Photogenerated Cl_2 and H_2 measured over two hours under one sun illumination. Inset shows Faradaic efficiency for H_2 and Cl_2 production. The error bars represent data collected for five different samples.

H_2 and O_2 were investigated using gas chromatography. Chlorine was swept from the electrolyte solution by slow helium (He) purge into a potassium iodide solution, and the amount of dissolved chlorine was then measured by Iodometric titration. Before the stability tests, the system was purged with a pure He stream for two hours. Near unity Faradaic efficiency was observed for H_2 production for all samples. Chloride oxidation runs carried using 2nm e-beam deposited Pt on FTO substrate at a constant current density of 2 mA/cm^2 is also provided for comparison. For the best performing $BiVO_4/WO_3$ electrode, a photocurrent-to-Cl_2 Faradaic efficiency of 85 percent was observed. No O_2 was detected during the reaction—reflecting that the slightly lower Faradaic efficiency obtained for Cl_2 production is due to the sampling method. This is also evident from the similar Faradaic efficiencies obtained from our control dark electrolysis runs using Pt electrocatalyst (Rassoolkhani et al. 2019).

3.2. Task 2.0. Fabricate Inorganic Electroactive Membranes

Two sub-tasks tasks were carried out using nanoporous AAO membranes as synthetic platforms to fabricate electroactive membranes. A schematic showing important geometrical of porous anodic alumina oxide membranes is shown below, along with SEM images (Figure 15).

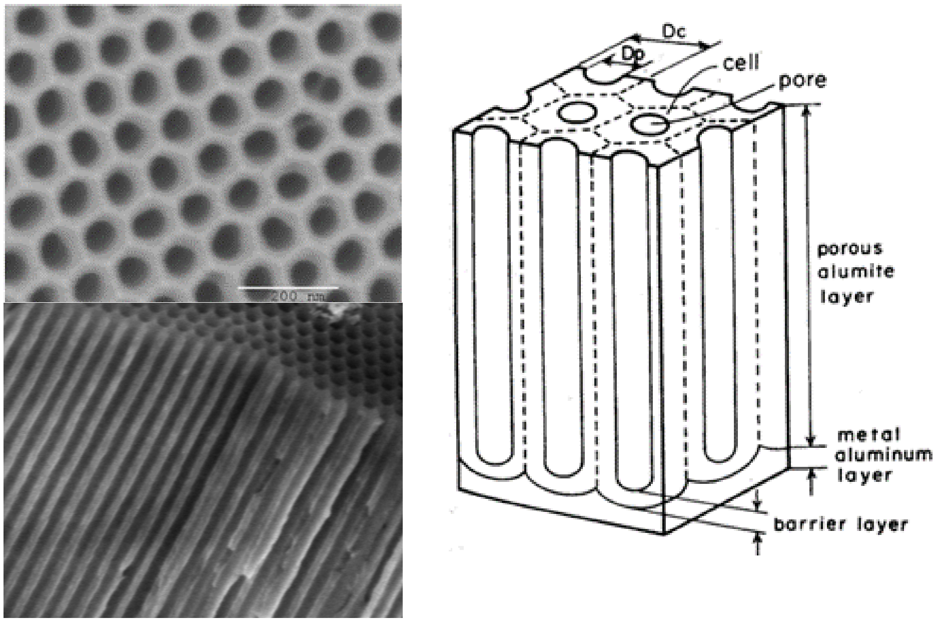

Figure 15.—Top and a cross-sectional view of porous anodic alumina oxide membrane made in-house.

3.2.1. Subtask 1. Grow Hollow Carbon Nanotubes

The first task was to grow hollow carbon nanotubes using a high-temperature carbonization process into the AAO to yield an enormous array (10^{10} pores/cm^2) of identical, aligned, and stable homogenous membranes with inner pore diameters less than 5 nm. Pore size, pore density, and thickness of AAO can be controlled by electrochemical/chemical etching parameters. The inner pore diameter of carbon nanotubes can be tuned by controlling conditions of the carbonization process (Figure 16). Details are given in Section 2. Technical Approach and Methods.

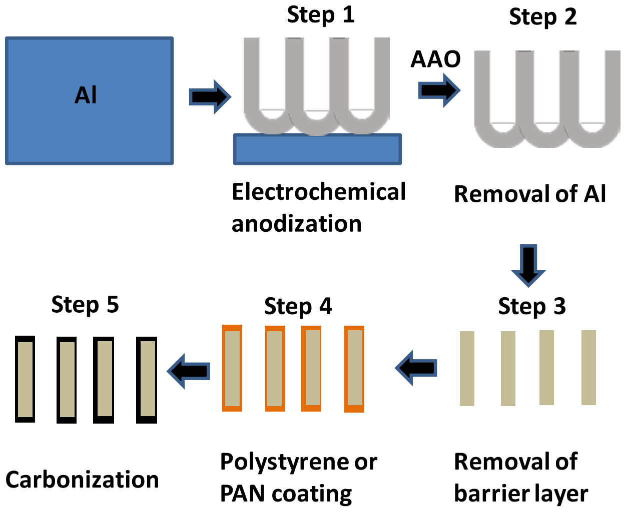

Figure 16.—Schematic showing the step-by-step synthetic procedure for carbon-based electrically conducting membranes.

3.2.2. Subtask 2. Provide Electroactive Carbon Coatings

After we synthesized the AAO with the desired pore size and pore density, we coated the inner walls and the surfaces of the alumina membrane with polystyrene suspended in dimethyl formamide by drop casting followed by carbonization at higher temperatures. The thickness of the coating was controlled by tuning the concentration of the polystyrene and carbonization temperature. Using the above strategy, we were successful in coating inner walls of alumina membranes (pore diameter of ~100 nm and thickness ~1 micron) with carbonized polystyrene to form hollow core-shell structures (Figure 17). The effective pore diameter of the coating was approximately 50nm.

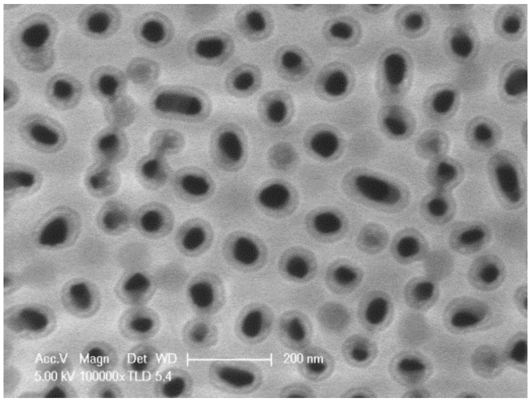

Figure 17.—Top-view SEM image of hollow polystyrene tubes formed inside porous alumina membrane.

3.2.3. Limitations of the Above Approach and Alternate Strategies

Although we were able to show synthetic feasibility of the proposed approach, we were unable to successfully fabricate electroactive carbon coatings inside alumina membranes with pore diameters less than 20 nm. This was due to:

(1) Clogging of smaller pore diameter alumina membranes during high-temperature carbonization

(2) Increased surface tension with decreasing pore diameter of alumina membranes resulting in incomplete polymer wetting

We identified a few strategies to address these issues, for example, use of low-surface tension polymers and improving the wettability of alumina pore walls using silane functionalization. However, we chose to pursue an alternate strategy of depositing nanoporous metal nanowires inside porous alumina templates as:

(1) Considerable knowledge exists on metal alloy electrodeposition and selective etching for metal nanopore fabrication, which can be readily extended for the proposed technology

(2) The pore sizes depend on the atomic ratio of the alloy segments and not on the starting pore diameter of the alumina membrane, allowing the use of commercial alumina membranes

We are mindful that using metals may ultimately limit the practical application of these materials due to concerns over cost and metal leaching. Nonetheless, the physical understanding that will be developed through this focused approach will serve as the basis for developing design principles for high-efficient electroactive membranes using cheaper, earth-abundant, and non-toxic materials. For example, one could employ similar strategies to electrodeposit conducting polymeric nanowires with metal inclusions (metal inclusions can then be selectively etched to realize porous conducting polymeric membranes), enabling the use of metal-free membranes to circumvent issues due to metal leaching.

3.2.4. Alternate Approach: Synthesis, Characterization, and Performance Evaluation of Nanoporous Metallic Membranes

A flowchart for the fabrication of nanoporous metallic electroactive membranes is shown in Figure 18.

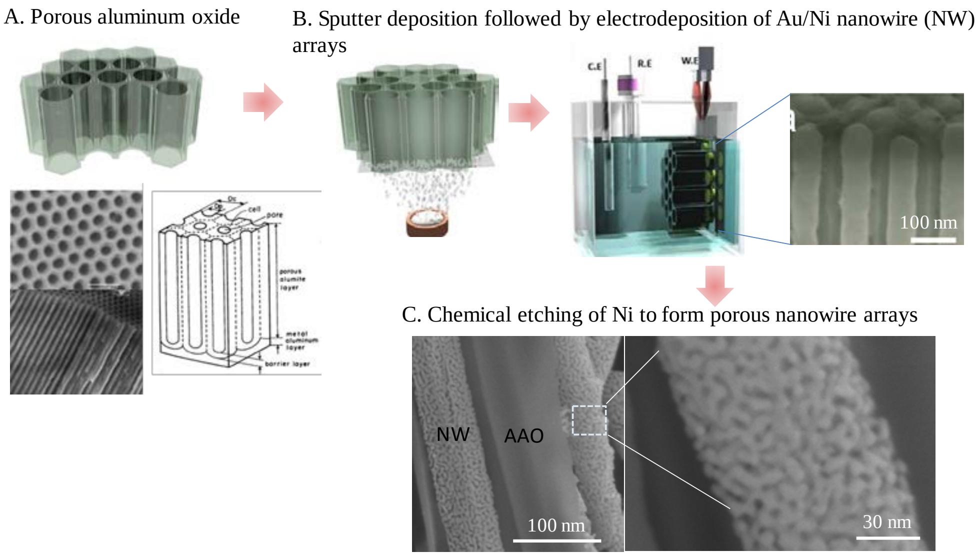

Figure 18.—Proposed flowchart for the fabrication of porous nanowire arrays. Shown here are steps A-C.

The fabrication steps included:

A. **Electrochemical anodization of aluminum** to form porous anodic aluminum oxide templates. Anodization voltages, temperature, and chemistries were tuned prescriptively to obtain desired pore size, pitch, and pore density. These are strategies that other groups and we have studied and used extensively. Our design goal is to create high pore density per unit membrane area (10^{10} pores/cm^2) to enable high ion-flux across the membranes. Membrane thickness was controlled by anodization time and would be sufficiently thin (<1 micron) to minimize overall cell resistance.

B. **Sputter deposition of Ni electrical backing layer followed by electrodeposition** of gold-nickel alloy nanowires. Electrolyte chemistries were tuned to obtain different atomic ratios of gold-nickel alloy nanowires. Figure 18 (Step B inset) shows the SEM image of $Au_{60}Ni_{40}$ nanowires obtained in our lab.

C. **Selective chemical etching of nickel** in concentrated nitric acid resulting in porous gold nanowire arrays. In Figure 18, the inset in Step C shows SEM images of porous gold nanowire arrays obtained after selective chemical etching. The pore sizes depend on the atomic ratio of the alloy segments. Our design goal for this task is to systematically tune the atomic ratios of nickel to gold to yield pore sizes from 2 nm to 5 nm that match the hydrodynamic diameters of the major ions (e.g., Na^+ and Cl^-) to be separated (i.e., typically less than 5 nm). This effort provided a systematic framework to fundamentally understand structure-property/activity correlation of these electroactive membranes for water treatment technologies.

D. **Low-temperature oxidation for tuning surface wettability.** Ideally, for separations, the membrane surface should be hydrophilic at the mouth of the pores to slow fouling (organic) and scaling (build-up of OH^- ions at the surface leading to precipitation) and hydrophobic at the inner walls for efficient ion-migration. The as-prepared nanoporous metal nanowire arrays are hydrophobic. To impart hydrophilicity at their mouth, a low-temperature air oxidation step with airflow parallel to the surface was employed, thereby exploiting the hydrophilicity of the resulting gold oxide. Flux rate, temperature, and time were optimized to spatially control (surface vs. inner walls of the alumina membrane) the hydrophobic/ hydrophilic properties of the membrane. Contact angle measurements were performed to measure surface wetting properties.

The above-proposed alternate fabrication approach was successfully used to routinely fabricate large area, nanoporous, gold membranes (Figure 19a). We tuned the pore sizes by controlling the etching time of the reactive metal (nickel or silver) (Figure 19b and Figure 19c).

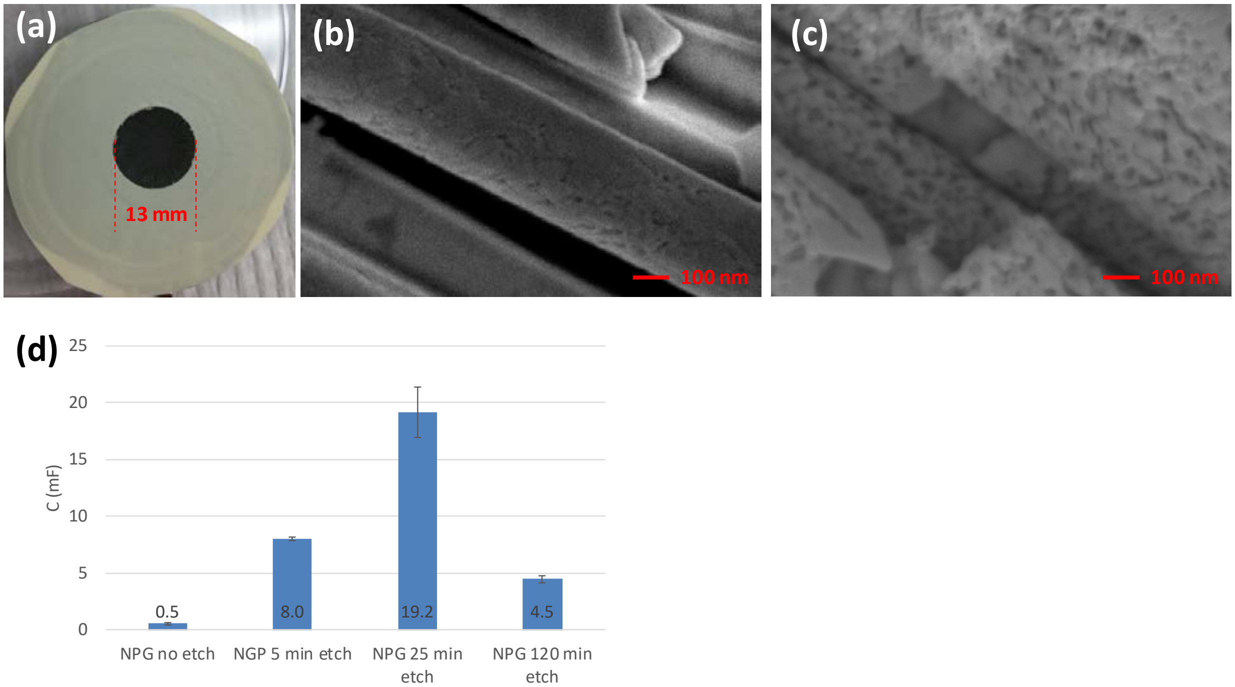

Figure 19.— (a) Digital photograph of a 13 mm nanoporous electroactive membrane synthesized in-house. SEM images of alloy nanowires etched for the different time duration (b) 5 minutes and (c) 120 minutes. (d) Electrochemical capacitance measurements of nanowire membranes for different etching times.

Figure 19d shows electrochemical capacitance measurements of the membranes as a function of the etching time. The capacitance measurements directly correlate with the electrochemically active surface area of the membranes. The active surface area increases with etching duration due to the formation of the nanopores. Samples etched for a longer duration, however, show a drop in capacitance value as larger size nanopores (>10 nm) start to form, effectively decreasing the overall surface area of the membranes. In the future, we will also use alternating current (AC) impedance spectroscopy measurements to understand the thickness of the double layer formed across these pores (a crucial parameter to control surface charge density) as a function of membrane potential and electrolyte concentration.

We explored the ability of the membranes to reject ions primarily by using potentiostatic approaches (i.e., controlling the ion-selectivity by injecting excess charges into the membrane). For example, excess negative charges can be created at the inner walls by applying a negative potential. Ions with the same charge will get repelled, and counter-ions will flow through. To carry out these measurements, we built a diffusion cell, in which a membrane was sandwiched between two glass cells (Figure 20a).

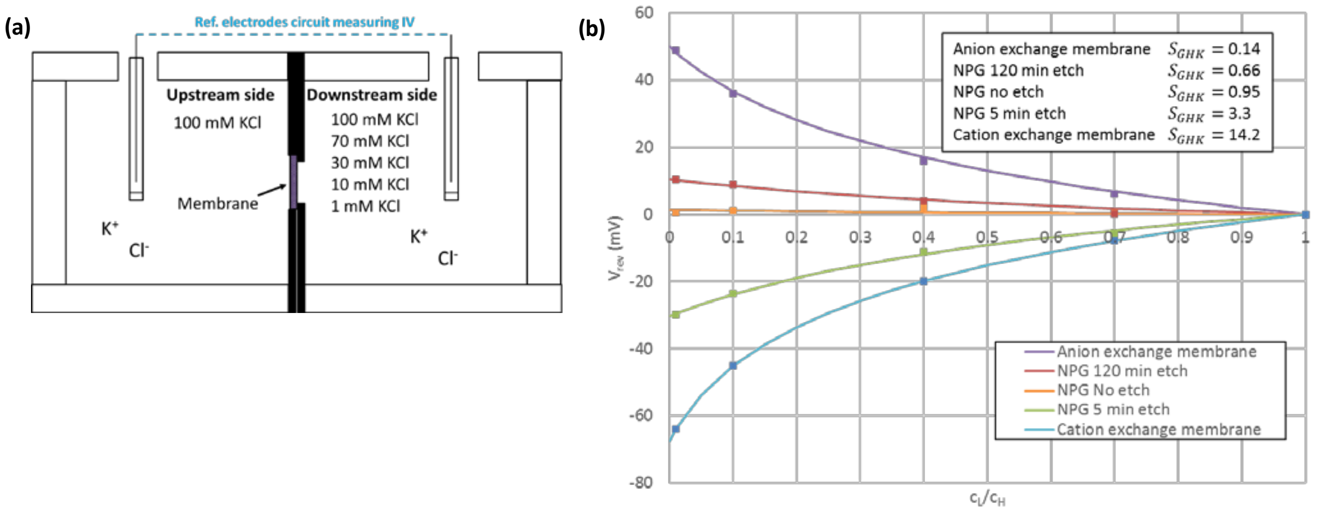

Figure 20.—(a) Schematic of the diffusion cell used for selectivity measurements. (b) Selectivity curves of commercial ion exchange membranes and in-house nanoporous membranes with various etch times showing increased cationic selectivity for the membrane etched for 5 minutes.

One-half of the diffusion cell (upstream side) had a higher electrolyte concentration, C_H and the other (downstream side) had a lower electrolyte concentration, C_L. The ratio of the downstream concentration to the upstream concentration is defined as the concentration ratio, C_L/C_H. Both halves of the diffusion cell were constantly stirred at 700 revolutions per minute (rpm). *IV* curves were obtained as a function of C_L/C_H concentration ratio ranging from 0.01 to 1 while sweeping from -150 mV to 150 mV between two Ag/AgCl reference electrodes on either side of the membrane. A reversal potential, V_{rev}, or the potential required for no current flow, arises when one species of ion diffuses faster than its co-ion. Therefore, by plotting V_{rev} for various concentrations of C_L/C_H, one could calculate the selectivity using the Nernst equation, as shown in Equation 8:

$$V_{rev} = \frac{k_B T}{e} \ln\left(\frac{S_{GHK}C_{high}+C_{low}}{S_{GHK}C_{low}+C_{high}}\right) \qquad (8)$$

Where:

S_{GHK} is the selectivity ratio defined as the ratio of the effective diffusion rates of the two mobile ions, K^+ and Cl^- as shown in Equation 9:

$$\frac{D^*_{K^+}}{D^*_{Cl^-}} = S_{GHK} \qquad (9)$$

As a control, the selectivity of a commercial cation exchange membrane and a commercial anion exchange membrane were first measured in the diffusion cell described above. The plots of V_{rev} versus C_L/C_H for the two commercial membranes and three synthesized nanoporous membranes are shown in Figure

20b. It should be noted that the membranes were not electrically charged for these measurements. Remarkably, the as-synthesized nanoporous membranes (here as-synthesized means no pre-treatment was done on the membranes) we fabricated showed preferential selectivity to cations without any applied bias (Figure 20, light grey trace)—suggesting that the as-synthesized membranes (i.e., without pre-treatment) were negatively charged. The as-synthesized membrane selectivity results were shown to vary based on the length of etching time (no etch, 5 minutes etch, or 120 minute etch) with membranes with larger pores (longer etching time) showing no preferential ion-selectivity.

Finally, to understand the effect of applied bias on ion-selectivity, the nanoporous membrane was connected to a third Ag/AgCl reference electrode placed on the upstream side of the cell through a source meter (Figure 21a).

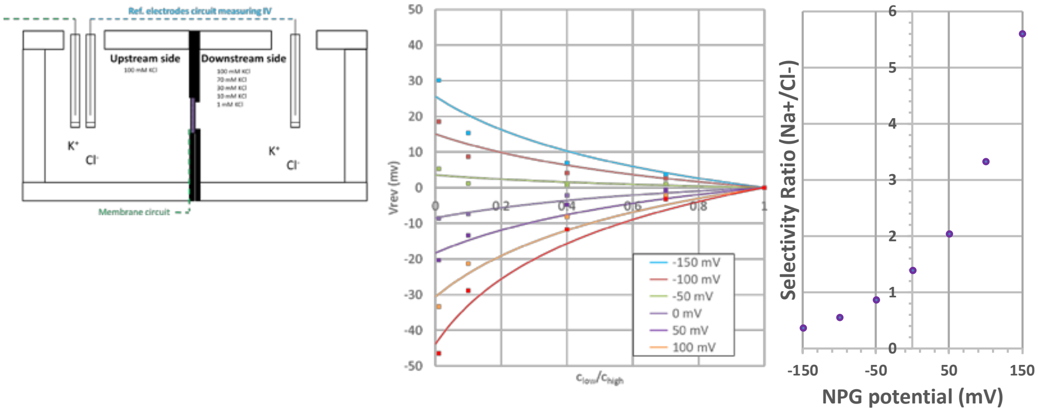

Figure 21.—(a) Schematic of diffusion cell used for selectivity measurements as a function of applied membrane bias. (b) reversal potential and (c) selectivity ratio curves as a function of membrane bias.

Like the above selectivity experiments, *IV* curves were collected across two Ag/AgCl reference electrodes over the same range of concentration ratios while the membrane potential was set to -150 mV to +150 mV vs. Ag/AgCl (in increments of 50 mV for a total of seven measurements per concentration ratio). The reversal potential curves and selectivity ratio for each membrane potential is shown in Figure 21b and Figure 21c. With no extensive optimization of the membrane structures, we were able to tune ion-selectivity of the membranes simply by tuning the membrane potential, with cation selectivity of about 5.5 and anion selectivity of about 3. Moreover, no change in ion selectivity was observed after performing these measurements repeated in brines containing a saturated concentration of Cl^- and SO_4^{2-} ions.

3.3. Task 3.0. Stand-Alone Lab Scale Treatment of Concentrate Brines

For the lab scale treatment of “ideal” NaCl brines, we purchased a commercial electrodialysis unit from PCCell-GMBH and retrofitted it to test our electrodes (Figure 22). To test the validity of our lab-scale treatment design, we initially performed demineralization experiments on electrodes in the presence of an external applied electric field.

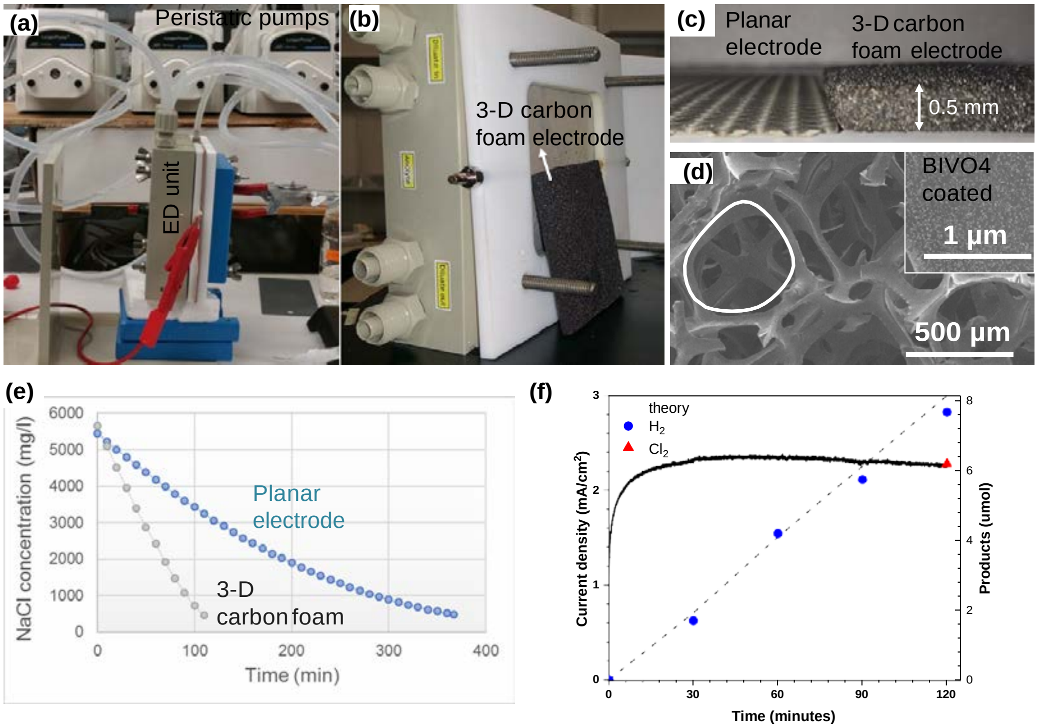

Figure 22.—(a) Digital photograph showing proposed treatment unit in operation. (b) A commercial unit from PCCell was custom modified to introduce proposed electrodes and electroactive membranes. (c) Digital photograph of planar and 3-D electrode used for treatment. (d) SEM image showing 3-D carbon foam coated with $BiVO_4$ (inset). (e) Preliminary results obtained using the proposed unit for commercial planar electrode and 3-D electrode. (f) Products produced during treatment of concentrated brines.

Two types of dark electrodes were employed for treatment:

i. Planar platinum coated titanium electrodes to mimic conventional treatment units

ii. Three- dimensional (3-D) carbon electrodes coated with photoactive solids to mimic proposed photoelectrode configuration

We monitored demineralization efficiency by measuring the conductivity of the treated brines as a function of time. Fuel and chemical products produced were quantified using GC (H_2), Iodometric (Cl_2), and pH measurement (NaOH). The demineralization results in 0.1 M NaCl as model brackish water feed is summarized in Figure 22.

The electrode compartment of the commercial unit was custom modified to introduce proposed photoelectrodes and electroactive membranes (Figure 22b). These electrodes were electrically contacted through a carbon cloth current collector. For the preliminary experiments, the 3-D carbon foam and commercial planar electrodes were 6 cm long by 6 cm wide, and the carbon foam and planar electrodes were 5 millimeters (mm) and 0.5 mm thick, respectively (Figure 22c). Figure 22d shows scanning electron microscopy (SEM) image of 3-D carbon foam coated with $BiVO_4$ nanoparticles. $BiVO_4$ was coated on carbon foam using procedures described in Section 2.4.2. The circled area in the SEM shows the pore diameter of the carbon foam used (~500 microns). A peristaltic pump was used to flow different concentrations of NaCl solution through dilute and concentrate compartments, and 0.1 M NaOH solution was flown across the electrode compartment. All solutions were circulated at a rate of 200 ml per minute. The demineralization progress was monitored by measuring current and total dissolved solids (TDS) concentration (Figure 22e) as a function of time. All demineralization experiments were carried out at the constant operating potential of 1.5 V with a total feed volume of 350 ml.

For three-dimensional (3-D) electrodes, an average current of 600 mA (5 mA/cm^2) was obtained with 100 minutes of operation, yielding a 95 percent demineralization efficiency ([initial concentration – final concentration]/initial concentration), 93 percent water recovery rate, and 94 percent current efficiency. In comparison, state-of-the-art planar electrodes (Figure 22e, blue trace) required about five hours to achieve a 90 percent demineralization efficiency, a 3-fold increase in demineralization time. Further, the current efficiency and water recovery rate were 15 and 10 percent lower than the 3-D electrodes used for this study.

Figure 22f shows the H_2 and Cl_2 produced from the brine treatment. These preliminary results provide a proof-of-concept experimental framework for quantitatively analyzing the experimental approach and testing the preliminary hypothesis that 3-D electrodes coated with photoactive solids offer high demineralization rates with improved current efficiency, water recovery percentage, and fuel and chemical production compared to state-of-the-art planar electrodes.

An external applied electric field was still needed for continuous operations. To overcome this challenge, we developed a stand-alone photoelectrochemical brine management unit, which uses the 3D photoactive electrodes in tandem with a triple-junction a-Si solar cells to truly perform the entire operation using sunlight as the sole energy input. This is termed a photovoltaic (PV) and photoelectrochemical (PEC) tandem device.

3.3.1. Achieving Self-Biased Operation of 3D Electrodes in Tandem with Other Photovoltaics

To provide the necessary bias to drive brine management using sunlight as the only energy input, we constructed a 3j a-Si tandem device using triple-junction amorphous silicon solar cell, as shown in Figure 23a. 3j a-Si is a promising candidate for tandem devices because of its low-cost, high photo potential and decent short-circuit current densities. Advantages of multijunction architecture are that the junctions can be designed for maximum absorbance across the solar spectrum (Figure 23b) and that the photovoltages add in series to achieve high potentials (Figure 23c). For example, the triple-junction a-Si solar cells shown in Figure 23a has a photopotential of 2.2 V.

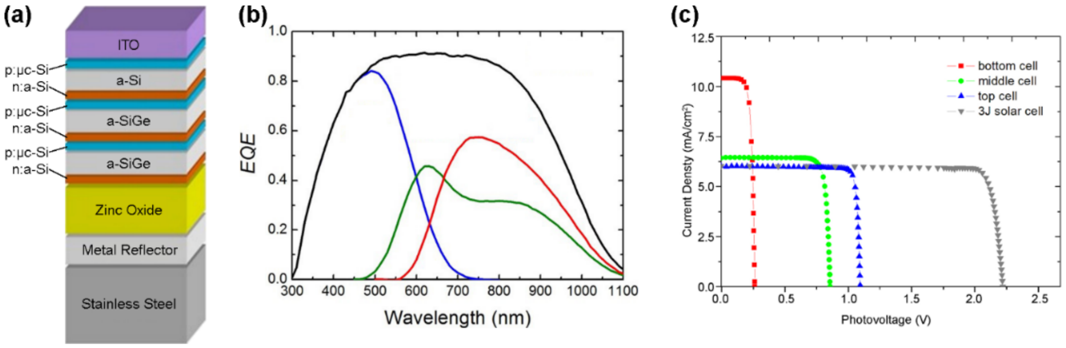

Figure 23.—(a) Diagram of thin film construction of the solar cell. (b) Absorption spectra of the three solar cell layers (black line is the sum of all absorption). Figure a and b provided by a commercial cell provider. (c) Photovoltage of individual cells and the total potential of the 3-in SC (adapted from manufacturer).

The PV-PEC device used a beam splitter to separate a standard solar cell (1 sun) into two light beams (Figure 24a). The simulated solar illumination was first obtained by passing light from a 300-W Xe arc lamp through a water filter (infrared filter), neutral density filters, or an AM 1.5-G filter. The power density of the incident light was calibrated to 100 mW/cm^2 by using a thermopile detector. This standard solar light was separated into two beams by a beam splitter (520 nm). The light beam (<520 nm) was used for testing the performance of PEC cells, and the other light beam was used for measuring the performance of 3j a-Si solar cells. Figure 24b shows the actual set-up of the entire unit. We were able to obtain a solar-to-H2 production efficiency of about 2 percent using the proposed tandem design with room for further improvement in the future. A stability test of the tandem device was also performed over 6 hours of operation. Although no device instability was obtained from morphological inspection, the amount of Cl_2 produced decreased by about 10 percent.

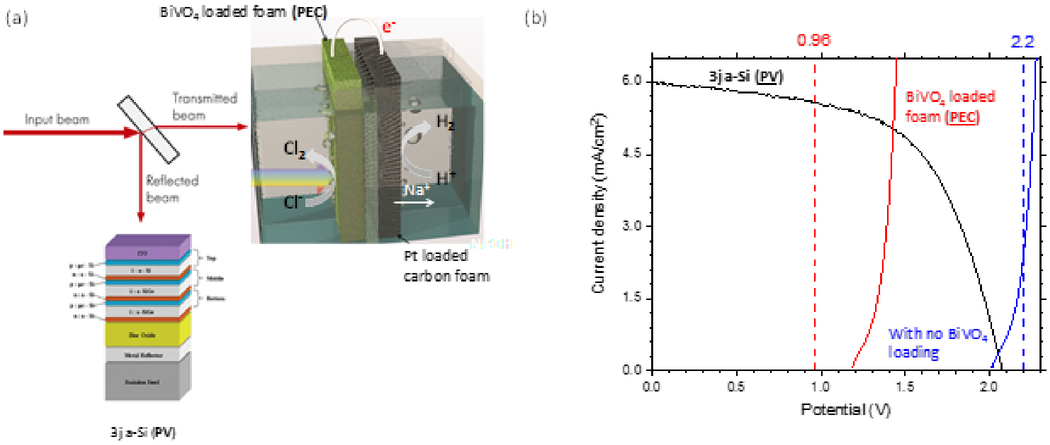

Figure 24.—(a) Configuration of a PV-PEC tandem PEC device design. (b) Current density-potential curves of the PV device and BiVO4 photoanode measured at one sun.

3.4. Task 4.0. Perform First Order Technoeconomic Assessment

The overall breakdown of system components for the technoeconomic analysis is shown in Figure 25.

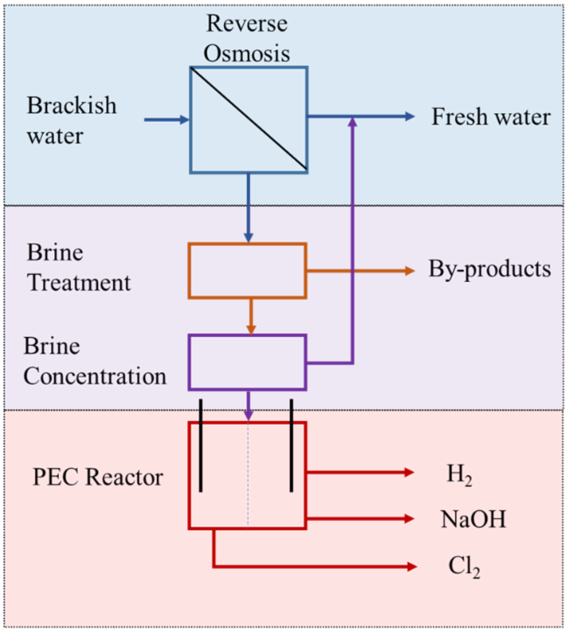

- Desalination Design Capacity: 2 MGD
- Operating factor: 0.5
- NaCl feed concentration: 1.2% w/w
- **Fresh water production cost: $0.35/m³**
- Recovery factor: 75%

- **Treatment and concentration cost: $2/m³**
- Exit NaCl concentration: 12% w/w
- Byproduct sales: $0/m³
- Recovery factor : 75%

- **Baseline PEC reactor energy efficiency: 5%**
- Selling price of H_2: $2/kg-$H_2$
- Selling price of Cl_2: $0.253/kg-$H_2$
- Selling price of 40% w/w NaOH: $0.125/kg-$H_2$

Figure 25.—Individual system components considered for technoeconomic assessment.

For brackish water desalination and brine treatment unit components, the cost was assumed based on prior reports. This report mainly details the technoeconomic assessment of the PEC reactor component. The baseline parameters for technoeconomic assessment of the PEC reactor component is provided in Figure 26. The plant lay out for the baseline case is shown in Figure 27.

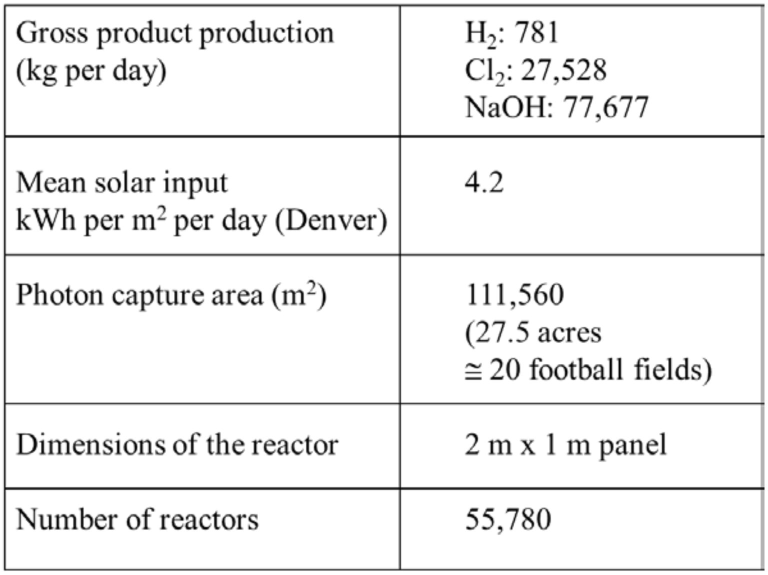

Gross product production (kg per day)	H_2: 781 Cl_2: 27,528 NaOH: 77,677
Mean solar input kWh per m^2 per day (Denver)	4.2
Photon capture area (m^2)	111,560 (27.5 acres ≅ 20 football fields)
Dimensions of the reactor	2 m x 1 m panel
Number of reactors	55,780

Figure 26.— Photoelectrochemical zero liquid discharge plant parameters – baseline case.

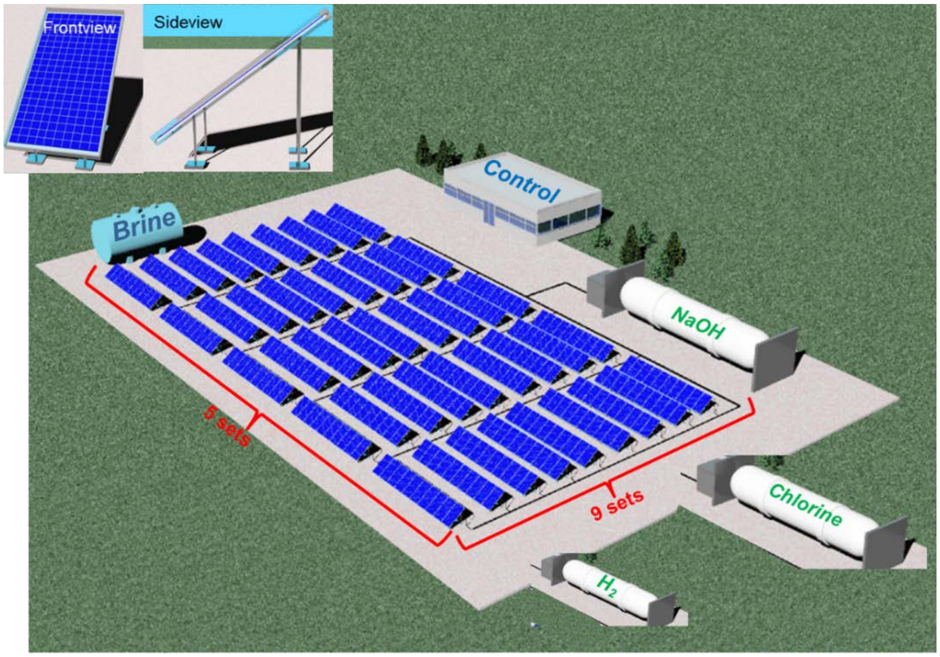

Figure 27.— Plant lay out for the baseline case.

The direct capital cost estimate breakdown and the discrete cashflow position chart is shown in Figure 28 and Figure 29. The project results in a positive net present value for a plant operation of 20 years and a fresh water production cost of $0.35/m^3. This cost is similar to the fresh water production cost obtained from RO desalination plants without a concentrate treatment unit—indicating that the high-value chemicals generated from the proposed design enable the proposed concentrate management approach to be profitable without increasing the fresh water production cost.

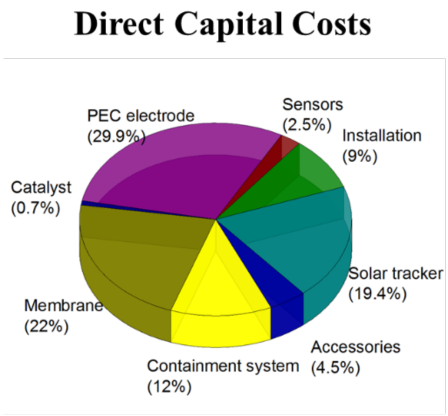

Parameter	Results
Solar-to-product conversion efficiency (Energy efficiency)	10%
Plant size (Concentrated brine)	0.05MGD
Photon capture area	55780 m^2
PEC electrode cost	$30/m^2
Electrode lifetime	2 years
Membrane cost	$12/m^2
Membrane lifetime	5 years
Total capital cost	$9.8 million
Replacement cost	~$0.94 million/year
Revenue from sales	$6.3 million/year

Figure 28.—Breakdown of direct capital cost with a table showing a summary of results for the baseline case.

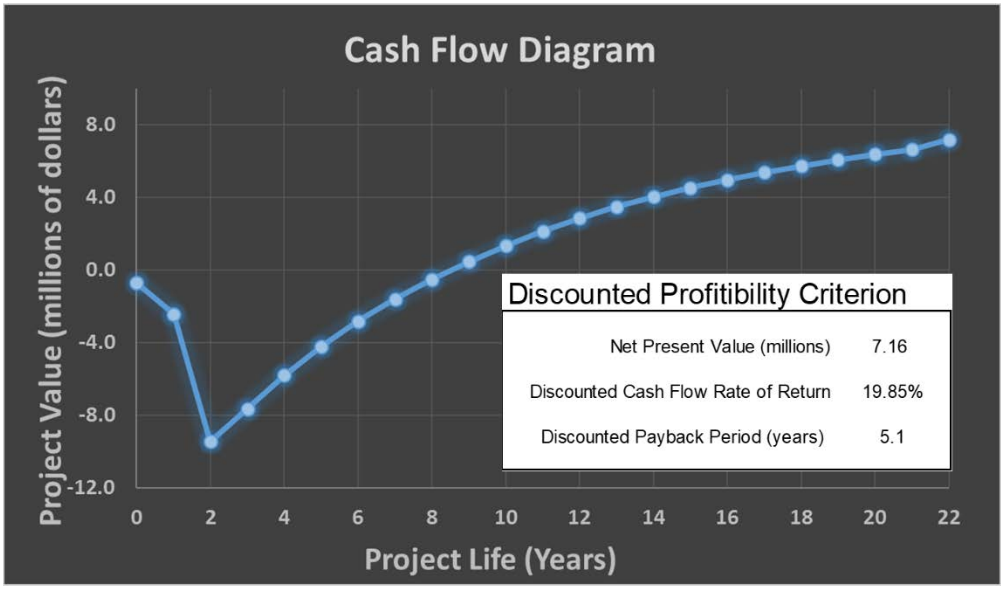

Figure 29.—A discounted cash flow diagram showing the profitability of the proposed approach.

4. Conclusions and Recommendations

This study provided preliminary “proof-of-concept” data demonstrating the operational feasibility of this solar photoelectrochemical process for concentrate management. Notable technological advances made during this period are summarized below.

4.1. Technological Advances

4.1.1. Development and Stable Operation of Novel Photoelectrodes for Cl_2 and H_2 Evolution

Strategies to synthesize and fabricate semiconductor electrodes made of earth-abundant non-toxic materials (tin sulfide and bismuth vanadate) were developed and characterized for solar driven H_2 and Cl_2 production.

For H_2 production under acidified sodium chloride electrolyte, we used p-type tin sulfide. This was chosen because of its favorable interfacial energetics for proton reduction, narrow band-gap (~1.1 eV), high absorption coefficient, and earth abundance. Highly photoactive tin sulfide nanoplatelets were fabricated by low-cost chemical bath deposition. Protected by atomic-layer-deposited titanium oxide layer, the best performing tin sulfide photocathodes produced H_2 with photocurrent densities reaching 2.5 mA/cm^2 at the reversible hydrogen electrode (RHE) potential under simulated visible light illumination ($\lambda > 500$ nm, $P_{in} = 80$ mW cm^{-2}). The internal quantum efficiency averaged over the entire solar spectrum at 0 V vs. RHE was about 13 percent. This is the highest photocurrents and quantum efficiency reported for this class of materials.

For the photoelectrochemical Cl_2 production from an acidified sodium chloride solution, we used bismuth vanadate (n-$BiVO_4$). A major challenge here was to protect the semiconductors from corrosion due to chloride ion oxidation. To prevent photo-corrosion of bismuth vanadate during electrochemical operation, an amorphous tungsten oxide (WO_3) protective layer was electrochemically deposited on the nanoporous $BiVO_4$. The best performing bismuth vanadate/tungsten oxide showed more than 100 hours of stable operation for chlorine production at two mA/cm^2. The synthesized materials were also tested in concentrated brines from BGNDRF, and similar performance metrics (quantum efficiency >10%, stability > 100 hours) were obtained upon sunlight illumination.

4.1.2. Development and Performance Evaluation of Novel Inorganic, Electrically Conducting, Fouling-resistant Membranes

We also developed a generalized framework for the synthesis of ultrathin monodisperse, porous inorganic membranes with electrically conducting coatings that can be electrically triggered and tailored to increase monovalent ion selectivity and transport. Two types of inorganic membranes were synthesized and characterized:

(1) Hollow inorganic membrane architecture, consisting of vertical arrays of carbon nanotubes inside porous anodic aluminum oxide (AAO) membranes.
(2) Porous inorganic membrane architectures are consisting of vertical arrays of nanoporous metal nanowires inside AAO membranes.

While not proposed initially, we synthesized electroactive nanoporous metal membrane architecture due to the difficulty in controlling the pore diameter below 10nm for carbon-coated membranes. Further, the nanoporous metal membranes demonstrated superior performance for selective passage of cations or anions by controlling the membrane surface charge density as a function of the applied bias. The non-optimized membranes showed cation selectivity (K^+/Cl^-) of ~6 and anion selectivity (Cl^-/K^+) of ~3 depending on the magnitude of the applied bias. To our knowledge, this was the first demonstration of electroactive nanoporous membranes with tunable ion exchange properties.

4.2. Outcomes

Because of the significant technological and societal relevance of the proposed problem, the project generated widespread interest within and beyond the scientific community as summarized below.

Innovation: We filed a United States provisional patent application filed for the technology has also been filed (invention Disclosure Ref. No. 2016-023) and submitted three invention disclosures to the University of Iowa. During the project agreement period, we filed multiple disclosures both on the overall process and individual components (electrodes and membranes).

Dissemination: We published a manuscript highlighting the photocathode performance in *Advanced Science* last year (Adv.Sci.2018, 5, 1700362; IF-9.034). A manuscript highlighting photoanode performance is submitted to *Nature Nanotechnology* and manuscript highlighting the electrode architecture innovation for hydrogen evolution reaction is submitted to *ACS Applied Nanomaterials*. Two manuscripts are currently under preparation highlighting the synthetic breakthroughs and performance evaluation of electroactive ion-exchange membranes. The results were also disseminated in the form of oral and poster presentations (7 total) at various national and international conferences, including the American Institute of Chemical Engineers (AIChE) and Electrochemical Society (ECS).

4.3. Recommended Next Steps

Although our studies within this agreement achieved several significant accomplishments on the individual component level, strategies for integrating these components into a complete and functioning system are needed to move towards commercialization. Specific questions that must be addressed to close existing knowledge gaps include:

1. What catalyst loadings, stabilization coating thickness, and ion-transport approaches will result in the most energy efficient and stable production of fuels and chemicals from concentrate brines?

2. Does the new reactor design strategy meet the performance metrics and cost targets needed for wide scale market adoption? Research in these areas needs to be performed to push this technology further towards large scale commercialization.

Currently, no generalized framework exists for designing and evaluating wireless solar PEC device for concentrate brine management. Specifically, our knowledge on catalyst loading on light absorbers, ion transport resistance, and its overall effect on resource recovery from concentrate brine for large scale devices is still very poor.

For example, a large-scale solar-driven membrane concentrate plant requires four key components: a light absorber (that converts photon energy into electrical or chemical energy), fuel forming electrocatalysts (that converts H+ and Cl- ions to H_2 and Cl_2), stabilization coatings (to protect light absorbers from chemical and photoelectrochemical corrosion), and membranes (to separate products and to prevent ion imbalance). Many devices and system configurations can be organized to include these individual components concerning their technology maturity and cost (Figure 30). The most common and technologically mature concept involves commercial photovoltaic (PV) modules connected to discrete concentrate treatment units (Figure 30a).

Several assessments on the cost and eventual viability of such device designs in recent literature indicate that the balance of plant (BOP) cost associated with such discrete systems are prohibitive for wide-scale adoption. The second-most promising design from a cost perspective is to integrate sunlight powered electrode assemblies directly into the concentrate treatment unit to generate products of interest (Figure 30b; our design in this study). In this design, the photocathode and photoanode are placed in different compartments separated physically and ionically by membranes and shorted electrically using metallic wires (“wired” design).

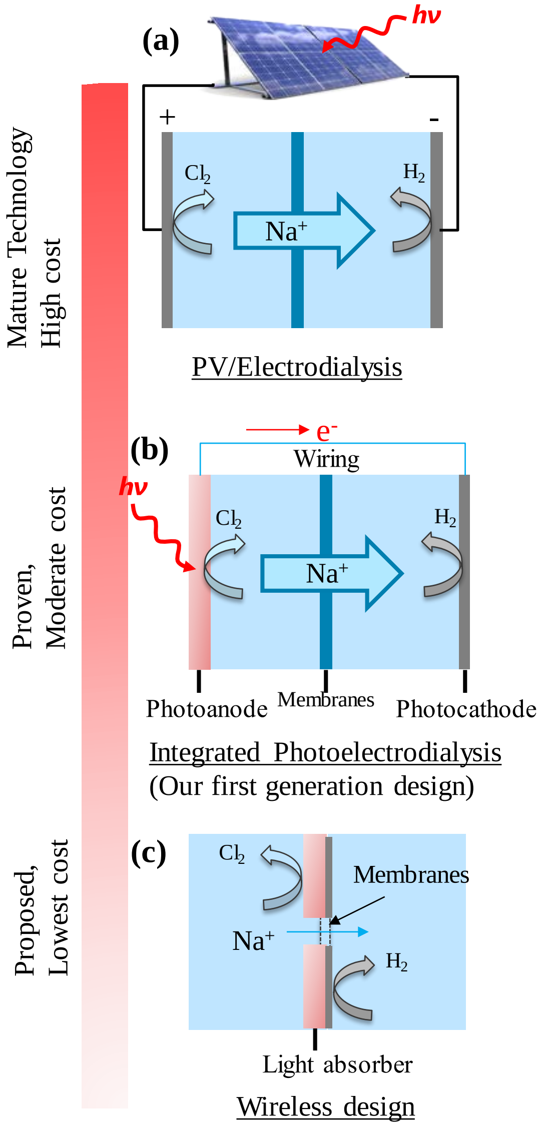

Figure 30.—Schematic showing the technology direction for the proposed approach.

The preliminary technoeconomic analysis of this system showed significant promise concerning project profitability on a 20-year lifetime basis. However, with cost as the major constraint for these technologies, a “wireless” layout (Figure 30c)—which mimics natural photosynthetic process—is needed to further simply the overall cell design and minimize the balance of plant cost by eliminating the use of wires. In a “wireless” layout, photoelectrodes, catalysts, stabilization coatings, and membranes are all integrated into a single monolithic device. Such a “wireless” design strategy has shown to reduce BOP cost by another 2 to 3-fold compared to “wired” design.

References

Avellaneda, D.; Nair, M. T. S.; and Nair, P. K., 2009. Photovoltaic structures using chemically deposited tin sulfide thin films. Thin Solid Films, 517 (7), 2500-2502.

Avlonitis, S. A.; Kouroumbas, K.; and Vlachakis, N., 2003. Energy consumption and membrane replacement cost for seawater RO desalination plants. Desalination, 157 (1–3), 151-158.

Bai, A.; Hu, C.-C.; Yang, Y.-F.; and Lin, C.-C., 2008. Pore diameter control of anodic aluminum oxide with ordered array of nanopores. Electrochimica Acta, 53 (5), 2258-2264.

Baltrusaitis, J.; Hu, Y.-S.; McFarland, E. W.; and Hellman, A., 2014. Photoelectrochemical Hydrogen Production on α-Fe2O3 (0001): Insights from Theory and Experiments. ChemSusChem, 7 (1), 162-171.

Bowen, W. R.; Kingdon, R. S.; and Sabuni, H. A. M., 1989. Electrically enhanced separation processes: the basis of *in situ* intermittent electrolytic membrane cleaning (IIEMC) and in situ electrolytic membrane restoration (IEMR). Journal of Membrane Science, 40 (2), 219-229.

Cesar, I.; Kay, A.; Gonzalez Martinez, J. A.; and Grätzel, M., 2006. Translucent Thin Film Fe2O3 Photoanodes for Efficient Water Splitting by Sunlight: Nanostructure-Directing Effect of Si-Doping. Journal of the American Chemical Society, 128 (14), 4582-4583.

Chen, W.; Wu, J.-S.; and Xia, X.-H., 2008. Porous Anodic Alumina with Continuously Manipulated Pore/Cell Size. ACS Nano 2 (5), 959-965.

Cheng W, Singh N, Elliott W, Mubeen S et al. 2017. Earth-Abundant Tin Sulfide-Based Photocathodes for Solar Hydrogen Production. Adv Sci. 5(1):1700362.

Davies, T. A., 2005. Water Desalination Process and Apparatus. PCT/US2005/032419.

Elimelech, M. and Phillip, W. A., 2011. The Future of Seawater Desalination: Energy, Technology, and the Environment. Science, August 5, 2011. Volume 333. http://science.sciencemag.org/content/sci/333/6043/712.full.pdf.

Furneaux, R. C.; Rigby, W. R.; and Davidson, A. P., 1989.The formation of controlled-porosity membranes from anodically oxidized aluminum. Nature 1989, 337 (6203), 147-149.

Garcıa, A. and Rodriguez, L., 2003. Renewable energy applications in desalination: state of the art. Solar Energy 2003, 75 (5), 381-393.

Greenlee, L. F.; Testa, F.; Lawler, D. F.; Freeman, B. D.; and Moulin, P., 2010. The effect of antiscalant addition on calcium carbonate precipitation for a simplified synthetic brackish water reverse osmosis concentrate. Water Research, 44 (9), 2957-2969.

Hongtao, L.; Yan, L.; Zan, W.; and Ping, H., 2010. Facile synthesis of monodisperse, size-tunable SnS nanoparticles potentially for solar cell energy conversion. Nanotechnology, 21 (10), 105707.

Hu, B.; Wang, K.; Wu, L.; Yu, S.-H.; Antonietti, M.; and Titirici, M.-M., 2010. Engineering Carbon Materials from the Hydrothermal Carbonization Process of Biomass. Advanced Materials, 22 (7), 813-828.

Jagannadh, S. N. and Muralidhara, H. S., 1996. Electrokinetics Methods to Control Membrane Fouling. Industrial & Engineering Chemistry Research, 35 (4), 1133-1140.

Jaramillo, R.; Steinmann, V.; Yang, C.; Hartman, K.; Chakraborty, R.; Poindexter, J. R.; Castillo, M. L.; Gordon, R.; and Buonassisi, T., 2015. Making Record-efficiency SnS Solar Cells by Thermal Evaporation and Atomic Layer Deposition. (99), e52705.

Johnson, J. B.; Jones, H.; Latham, B. S.; Parker, J. D.; Engelken, R. D.; and Barber, C., 1999. Optimization of photoconductivity in vacuum-evaporated tin sulfide thin films. Semiconductor Science and Technology, 14 (6), 501.

Karagiannis, I. C. and Soldatos, P. G., 2008. Water desalination cost literature: review and assessment. Desalination, 223 (1–3), 448-456.

Kesieme, U. K.; Milne, N.; Aral, H.; Cheng, C. Y.; and Duke, M., 2013. Economic analysis of desalination technologies in the context of carbon pricing, and opportunities for membrane distillation. Desalination, 323, 66-74.

Khawaji, A. D.; Kutubkhanah, I. K.; and Wie, J.-M., 2008. Advances in seawater desalination technologies. Desalination, 221 (1–3), 47-69.

Kim, S. J.; Ko, S. H.; Kang, K. H.; and Han, J., 2010. Direct seawater desalination by ion concentration polarization. Nat Nano, 5 (4), 297-301.

Krol, J. J.; Wessling, M.; and Strathmann, H., 1999. Concentration polarization with monopolar ion exchange membranes: current–voltage curves and water dissociation. Journal of Membrane Science, 162 (1–2), 145-154.

Kyotani, T., 2000. Control of pore structure in carbon. Carbon, 38 (2), 269-286.

Lee, J.; Mubeen, S.; Ji, X.; Stucky, G. D.; and Moskovits, M., 2012. Plasmonic Photoanodes for Solar Water Splitting with Visible Light. Nano Letters, 12 (9), 5014-5019.

Logan, J., C. Marcy, J. McCall, et al., 2017. Electricity Generation Baseline Report. National Renewable Energy Laboratory. https://www.nrel.gov/docs/fy17osti/67645.pdf.

Mathews, N. R.; Anaya, H. B. M.; Cortes-Jacome, M. A.; Angeles-Chavez, C.; and Toledo-Antonio, J. A., 2010. Tin Sulfide Thin Films by Pulse Electrodeposition: Structural, Morphological, and Optical Properties. Journal of the Electrochemical Society, 10, 157 (3), H337-H341.

Masuda, H. and Fukuda, K., 1995. Ordered Metal Nanohole Arrays Made by a Two-Step Replication of Honeycomb Structures of Anodic Alumina. Science 1995, 268 (5216), 1466-1468.

Mathioulakis, E.; Belessiotis, V.; and Delyannis, E., 2007. Desalination by using alternative energy: Review and state-of-the-art. Desalination, 203 (1–3), 346-365.

Mubeen, S.; Lee, J.; Singh, N.; Kramer, S.; Stucky, G. D.; and Moskovits, M., 2013. An autonomous photosynthetic device in which all charge carriers derive from surface plasmons. Nat Nano, 8 (4), 247-251.

Mubeen, S. et al. 2017. Wo2018119280a1 - Apparatus And Method For Three-Dimensional Photo-electrodialysis. https://patents.google.com/patent/WO2018119280A1/en

Murphy, G. W., 1981. Desalination by Photoelectrodialysis. II. Journal of The Electrochemical Society 1981, 128 (8), 1819-1821.

Ning, J.; Men, K.; Xiao, G.; Wang, L.; Dai, Q.; Zou, B.; Liu, B.; and Zou, G., 2010. Facile synthesis of iv-vi SnS nanocrystals with shape and size control: Nanoparticles, nanoflowers and amorphous nanosheets. Nanoscale, 2 (9), 1699-1703.

Nishinaga, O.; Kikuchi, T.; Natsui, S.; and Suzuki, R. O., 2013. Rapid fabrication of self-ordered porous alumina with 10-/sub-10-nm-scale nanostructures by selenic acid anodizing. Scientific Reports 2013, 3, 2748.

Noguchi, H.; Setiyadi, A.; Tanamura, H.; Nagatomo, T.; and Omoto, O., 1994. Characterization of vacuum-evaporated tin sulfide film for solar cell materials. Solar Energy Materials and Solar Cells 1994, 35, 325-331.

Peñate, B. and García-Rodríguez, L., 2012. Current trends and future prospects in the design of seawater reverse osmosis desalination technology. Desalination, 284, 1-8.

Ramakrishna Reddy, K. T.; Koteswara Reddy, N.; and Miles, R. W., 2006. Photovoltaic properties of SnS based solar cells. Solar Energy Materials and Solar Cells, 90 (18–19), 3041-3046.

Rassoolkhani A, Cheng W, Mubeen S, et al. 2017. Nanostructured Bismuth Vanadate/Tungsten Oxide Photoanode For Chlorine Production With Hydrogen Generation At The Dark Cathode. Communications Chemistry (accepted). 10.1038/s42004-019-0156-x.

Redepenning, J. and Anson, F. C., 1987. Permselectivities of polyelectrolyte electrode coatings as inferred from measurements with incorporated redox probes or concentration cells. The Journal of Physical Chemistry, 91 (17), 4549-4553.

Sajeesh, T. H.; Warrier, A. R.; Kartha, C. S.; and Vijayakumar, K. P., 2010. Optimization of parameters of chemical spray pyrolysis technique to get n and p-type layers of SnS. Thin Solid Films, 518 (15), 4370-4374.

Semiat, R., 2008. Energy Issues in Desalination Processes. Environmental Science and Technology, 42 (22), 8193-8201.

Shrestha, E.; Ahmad, S.; Johnson, W.; Shrestha, P.; and Batista, J. R., 2011. Carbon footprint of water conveyance versus desalination as alternatives to expand water supply. Desalination, 280 (1–3), 33-43.

Steinmann, V.; Jaramillo, R.; Hartman, K.; Chakraborty, R.; Brandt, R. E.; Poindexter, J. R.; Lee, Y. S.; Sun, L.; Polizzotti, A.; Park, H. H.; Gordon, R. G.; and Buonassisi, T., 2014. 3.88% Efficient Tin Sulfide Solar Cells using Congruent Thermal Evaporation. Advanced Materials, 26 (44), 7488-7492.

Singh, N.; Mubeen, S.; Lee, J.; Metiu, H.; Moskovits, M.; and McFarland, E. W., 2014. Stable electrocatalysts for autonomous photoelectrolysis of hydrobromic acid using single-junction solar cells. Energy & Environmental Science, 7 (3), 978-981.

Sivula, K.; Le Formal, F.; and Grätzel, M., 2011. Solar Water Splitting: Progress Using Hematite (α-Fe2O3) Photoelectrodes. ChemSusChem, 4 (4), 432-449.

Subramanian, B.; Sanjeeviraja, C.; and Jayachandran, M., 2001. Cathodic electrodeposition and analysis of SnS films for photoelectrochemical cells. Materials Chemistry and Physics, 71 (1), 40-46.

Suh, J. S. and Lee, J. S., 1999. Highly ordered two-dimensional carbon nanotube arrays. Applied Physics Letters, 75 (14), 2047-2049.

Sun, Y.; Cheng, H.; Gao, S.; Sun, Z.; Liu, Q.; Liu, Q.; Lei, F.; Yao, T.; He, J.; Wei, S.; and Xie, Y., 2012. Freestanding Tin Disulfide Single-Layers Realizing Efficient Visible-Light Water Splitting. Angewandte Chemie International Edition, 51 (35), 8727-8731.

Turek, M. 2003. Dual-purpose desalination-salt production electrodialysis. Desalination, 153 377-381.

Wagner, N., 2002. Characterization of membrane electrode assemblies in polymer electrolyte fuel cells using AC impedance spectroscopy. Journal of Applied Electrochemistry, 32 (8), 859-863.

Wangxi, Z.; Jie, L.; and Gang, W., 2003. Evolution of structure and properties of PAN precursors during their conversion to carbon fibers. Carbon, 41 (14), 2805-2812.

Yang, Y.; Zheng, G.; and Cui, Y., 2013. Nanostructured sulfur cathodes. Chemical Society Reviews, 42 (7), 3018-3032.

Zhang, X.; Yang, L.; Jiang, Y.; Yu, B.-B.; Zou, Y.-G.; Fang, Y.; Hu, J.-S.; and Wan, L.-J., 2013. Facile Solution Synthesis and Photoelectric Properties of Monolithic Tin(II) Sulfide Nanobelt Arrays. Chemistry – An Asian Journal, 8 (10), 2483-2488.

Zheng, G.; Yang, Y.; Cha, J. J.; Hong, S. S.; and Cui, Y., 2011. Hollow Carbon Nanofiber-Encapsulated Sulfur Cathodes for High Specific Capacity Rechargeable Lithium Batteries. Nano Letters, 11 (10), 4462-4467.

Zhou, X.; Yang, H.; Wang, C.; Mao, X.; Wang, Y.; Yang, Y.; and Liu, G., 2010. Visible Light Induced Photocatalytic Degradation of Rhodamine B on One-Dimensional Iron Oxide Particles. The Journal of Physical Chemistry C, 114 (40), 17051-17061.